

AD _____

GRANT NUMBER: DAMD17-93-J-3009

TITLE: Digital Mammography with Storage Phosphors
(Breast Cancer)

PRINCIPAL INVESTIGATOR(S): Chris C. Shaw, Ph.D.

CONTRACTING ORGANIZATION: University of Pittsburgh
Pittsburgh, Pennsylvania 15261-0001

REPORT DATE: January 1996

TYPE OF REPORT: Final

PREPARED FOR: U.S. Army Medical Research and Materiel Command
Fort Detrick, Frederick, Maryland 21702-5012

DISTRIBUTION STATEMENT: Approved for public release;
distribution unlimited

The views, opinions and/or findings contained in this report are
those of the author(s) and should not be construed as an official
Department of the Army position, policy or decision unless so
designated by other documentation.

19960304 039

DTIC QUALITY INSPECTED 1

REPORT DOCUMENTATION PAGE

*Form Approved
OMB No. 0704-0188*

Public reporting burden for this collection of information is estimated to average 1 hour per response, including the time for reviewing instructions, searching existing data sources, gathering and maintaining the data needed, and completing and reviewing the collection of information. Send comments regarding this burden estimate or any other aspect of this collection of information, including suggestions for reducing this burden, to Washington Headquarters Services, Directorate for Information Operations and Reports, 1215 Jefferson Davis Highway, Suite 1204, Arlington, VA 22202-4302, and to the Office of Management and Budget, Paperwork Reduction Project (0704-0188), Washington, DC 20503.

1. AGENCY USE ONLY (Leave blank)			2. REPORT DATE January 1996		3. REPORT TYPE AND DATES COVERED Final (1 Dec 92 - 30 Nov 95)	
4. TITLE AND SUBTITLE Digital Mammography with Storage Phosphors (Breast Cancer)			5. FUNDING NUMBERS DAMD17-93-J-3009			
6. AUTHOR(S) Chris C. Shaw, Ph.D						
7. PERFORMING ORGANIZATION NAME(S) AND ADDRESS(ES) University of Pittsburgh Pittsburgh, Pennsylvania 15261-0001			8. PERFORMING ORGANIZATION REPORT NUMBER			
9. SPONSORING/MONITORING AGENCY NAME(S) AND ADDRESS(ES) Commander U.S. Army Medical Research and Material Command Fort Detrick Frederick, Maryland 21702-5012			10. SPONSORING/MONITORING AGENCY REPORT NUMBER			
11. SUPPLEMENTARY NOTES						
12a. DISTRIBUTION/AVAILABILITY STATEMENT Approved for public release; distribution unlimited				12b. DISTRIBUTION CODE		
13. ABSTRACT (Maximum 200 words) An experimental computed radiography (CR) system was configured for high resolution imaging applications. The modulation transfer function (MTF) of the system was improved and demonstrated to well exceed that of commercial systems. Phantom images were used to evaluate and compare the CR system with a screen-film mammography system for their low contrast performance. The results show that the performance of the CR system is close to but slightly lower than that of the screen-film system. A ROC study based on phantom images was conducted to quantitatively compare the CR system with the screen-film system for the tasks of detecting simulated microcalcifications and masses. The results demonstrated that for detection of microcalcifications, the CR system is close to but slightly lower in performance. For detection of masses, the CR system seems to perform better than the screen-film system. The results of this project indicates that further improvement of the MTF may be necessary for application of CR to mammographic imaging. Such improvement may be achieved by redesigning and improving the CR screens.						

14. SUBJECT TERMS Digital Radiography, Mammography, Breast Imaging Computer Radiography, Storage Phosphor, Breast Cancer			15. NUMBER OF PAGES 69
			16. PRICE CODE
17. SECURITY CLASSIFICATION OF REPORT Unclassified		18. SECURITY CLASSIFICATION OF THIS PAGE Unclassified	
19. SECURITY CLASSIFICATION OF ABSTRACT Unclassified		20. LIMITATION OF ABSTRACT Unlimited	

GENERAL INSTRUCTIONS FOR COMPLETING SF 298

The Report Documentation Page (RDP) is used in announcing and cataloging reports. It is important that this information be consistent with the rest of the report, particularly the cover and title page. Instructions for filling in each block of the form follow. It is important to *stay within the lines* to meet *optical scanning requirements*.

Block 1. Agency Use Only (Leave blank).

Block 2. Report Date. Full publication date including day, month, and year, if available (e.g. 1 Jan 88). Must cite at least the year.

Block 3. Type of Report and Dates Covered.

State whether report is interim, final, etc. If applicable, enter inclusive report dates (e.g. 10 Jun 87 - 30 Jun 88).

Block 4. Title and Subtitle. A title is taken from the part of the report that provides the most meaningful and complete information. When a report is prepared in more than one volume, repeat the primary title, add volume number, and include subtitle for the specific volume. On classified documents enter the title classification in parentheses.

Block 5. Funding Numbers. To include contract and grant numbers; may include program element number(s), project number(s), task number(s), and work unit number(s). Use the following labels:

C - Contract	PR - Project
G - Grant	TA - Task
PE - Program Element	WU - Work Unit Accession No.

Block 6. Author(s). Name(s) of person(s) responsible for writing the report, performing the research, or credited with the content of the report. If editor or compiler, this should follow the name(s).

Block 7. Performing Organization Name(s) and Address(es). Self-explanatory.

Block 8. Performing Organization Report Number. Enter the unique alphanumeric report number(s) assigned by the organization performing the report.

Block 9. Sponsoring/Monitoring Agency Name(s) and Address(es). Self-explanatory.

Block 10. Sponsoring/Monitoring Agency Report Number. (If known)

Block 11. Supplementary Notes. Enter information not included elsewhere such as: Prepared in cooperation with...; Trans. of...; To be published in.... When a report is revised, include a statement whether the new report supersedes or supplements the older report.

Block 12a. Distribution/Availability Statement.

Denotes public availability or limitations. Cite any availability to the public. Enter additional limitations or special markings in all capitals (e.g. NOFORN, REL, ITAR).

DOD - See DoDD 5230.24, "Distribution Statements on Technical Documents."

DOE - See authorities.

NASA - See Handbook NHB 2200.2.

NTIS - Leave blank.

Block 12b. Distribution Code.

DOD - Leave blank.

DOE - Enter DOE distribution categories from the Standard Distribution for Unclassified Scientific and Technical Reports.

NASA - Leave blank.

NTIS - Leave blank.

Block 13. Abstract. Include a brief (*Maximum 200 words*) factual summary of the most significant information contained in the report.

Block 14. Subject Terms. Keywords or phrases identifying major subjects in the report.

Block 15. Number of Pages. Enter the total number of pages.

Block 16. Price Code. Enter appropriate price code (*NTIS only*).

Blocks 17. - 19. Security Classifications. Self-explanatory. Enter U.S. Security Classification in accordance with U.S. Security Regulations (i.e., UNCLASSIFIED). If form contains classified information, stamp classification on the top and bottom of the page.

Block 20. Limitation of Abstract. This block must be completed to assign a limitation to the abstract. Enter either UL (unlimited) or SAR (same as report). An entry in this block is necessary if the abstract is to be limited. If blank, the abstract is assumed to be unlimited.

FOREWORD

Opinions, interpretations, conclusions and recommendations are those of the author and are not necessarily endorsed by the US Army.

CS Where copyrighted material is quoted, permission has been obtained to use such material.

CS Where material from documents designated for limited distribution is quoted, permission has been obtained to use the material.

CS Citations of commercial organizations and trade names in this report do not constitute an official Department of Army endorsement or approval of the products or services of these organizations.

NA In conducting research using animals, the investigator(s) adhered to the "Guide for the Care and Use of Laboratory Animals," prepared by the Committee on Care and Use of Laboratory Animals of the Institute of Laboratory Resources, National Research Council (NIH Publication No. 86-23, Revised 1985).

NA For the protection of human subjects, the investigator(s) adhered to policies of applicable Federal Law 45 CFR 46.

NA In conducting research utilizing recombinant DNA technology, the investigator(s) adhered to current guidelines promulgated by the National Institutes of Health.

NA In the conduct of research utilizing recombinant DNA, the investigator(s) adhered to the NIH Guidelines for Research Involving Recombinant DNA Molecules.

NA In the conduct of research involving hazardous organisms, the investigator(s) adhered to the CDC-NIH Guide for Biosafety in Microbiological and Biomedical Laboratories.



PI - Signature Date

TABLE OF CONTENTS

FRONT COVER	1
SF 298 REPORT DOCUMENTATION	2
FOREWORD	3
TABLE OF CONTENTS	4
INTRODUCTION	5-6
SYSTEM MODIFICATION AND OPTIMIZATION	7
Theoretical Considerations	7-11
System Modifications	11-13
Measurement of Laser Beam Spot Size	13-16
System Configuration	16
SYSTEM CHARACTERIZATION	17
Modulation Transfer Function (MTF)	17-23
Detective Quantum Efficiency (DQE)	23-25
Quality Control	25-27
COMPARISON- PHANTOM IMAGES	28-30
COMPARISON- ROC STUDIES	31
Phantom Design	31-33
Image Acquisition	33
ROC Data Collection	33-34
ROC Data Analysis	34-37
COMPRESSION OF IMAGE DATA	38-41
CONCLUSIONS	42-43
REFERENCES	44-50

APPENDIX I	Specifications for the Resolution Bar Pattern
APPENDIX II	Specifications for the CIRS Breast Phantom
APPENDIX III	Specifications for the Anthropomorphic Breast Phantom
APPENDIX IV	Captions for attached films
APPENDIX V	“Joint Photographic Experts Group (JPEG) Compatiable Data Compression of Mammograms”, manuscript

INTRODUCTION

Breast cancer has been a major cause for death for women in the United States. Currently, the major tool for screening and diagnosing breast cancer is the X-ray mammography. With this technique, X-ray images of breasts at low kVp to produce reasonably high image contrast for detecting microcalcifications, masses and examining tissue structure of the breast. Because microcalcifications are generally small in size, high spatial resolution is required to image them with reasonable sharpness and contrast for detection. On the other hand, high detection efficiency is required to minimize X-ray exposure and therefore cancer risk to the breast while producing reasonable signal-to-noise ratio for detecting the subtle contrast of small calcifications as well as tumor masses. Current mammographic technique employs high resolution screen-film combination as the image detector and recording system. This system provides adequate spatial resolution and detection efficiency for the mammographic imaging tasks.

Although screen-film techniques have provided reasonable image quality for various applications, there are several drawbacks. First of all, screen-film combinations require accurate control of X-ray exposures to avoid over- or under-exposure. Thus, retakes due to incorrect exposures represent a significant ratio of all radiographs taken. This increases film consumption as well as patient exposures. Secondly, film images are typically displayed on viewing boxes with fixed contrast and brightness. They can not be enhanced or processed without first being digitized. Lastly, storage, retrieval and transport of films are becoming an increasingly serious problem when films have accumulated for years.

With recent advances of digital technology, the Picture Archival and Communication Systems have become technically and economically feasible for use in the radiology environment. Such systems are expected to significantly improve the management of radiological images. However, with such systems in use, it also becomes more important to have a high quality but economic technique for direct digital acquisition of projection radiography images. Various digital radiography techniques have been developed to acquire projection radiography images. Some of them went further to provide improved image quality by incorporating scatter rejection capability or using X-ray detectors of superior quantum efficiency. However, many of these techniques also are either too expensive to implement or suffer from poor spatial resolution. Among these digital radiography techniques, the storage phosphor imaging technique has evolved to be a promising candidate for large scale implementation of digital radiography capability in radiology environment.

Storage phosphor (SP) imaging is a technique of using metastable electron states to temporarily store X-ray exposure information and then using scanning laser beam to read out the latent image signal as light emitted when the electrons in the metastable state are excited and return to the ground state. Because the SP image plates can be housed and exposed in cassettes similar to those used in conventional screen-film radiography,

the SP imaging technique can be implemented without replacing the currently used X-ray equipment and with minimal training requirement for the technologists. Thus, it provides a convenient and economic way to incorporate digital radiography capability.

Although the SP imaging technique has been actively used in foreign countries for mammographic imaging applications, its applications in the United States have been limited to general radiography, particularly to chest imaging in the intensive care unit¹⁻⁷. Due to technical or marketing considerations, typical commercial SP imaging systems have been configured to use a pixel size ranging from 86 to 200 μm with a laser spot size of 100 μm or greater.⁸⁻¹⁰ Due to this limitation of the screen optics⁸⁻¹⁰, current commercial CR systems do not have sufficient spatial resolution capability for mammographic imaging applications^{92,93}. This practice poses limitations on the use of current commercial SP imaging systems for high resolution imaging applications, among which is the mammographic imaging.

Overall Goals

In this project, we propose to modify and optimize an experimental CR system for high resolution mammographic imaging applications. Image properties of the optimized system will be characterized by measuring the signal response, MTF and noise properties. A comprehensive comparison study based on phantoms will be conducted to evaluate and compare the CR technique with the conventional screen-film technique for detection of microcalcifications as well as low contrast soft tissue masses. Possibility for patient dose reduction will also be investigated. In an addendum to our proposal dated October 26, 1992, we also proposed to perform preliminary investigations on data compression of mammographic or similar types of images.

Main Tasks

The project consists of five major components: (1) system modification and optimization, (2) system characterization and quality control, (2) comparison study based on phantom images, (4) comparison study based on ROC studies and (5) image compression study. These tasks have largely been accomplished and will be described and discussed in details in the following sections.

1. SYSTEM MODIFICATION AND OPTIMIZATION

Theoretical Considerations

In storage phosphor imaging, the X-rays expose the SP image plates, leaving a two-dimensional distribution of trapped electron energy. This energy distribution is also referred to as the latent image signal. During image readout, the trapped electron energy is released by a scanning laser beam^{1,2,7}. The blurring processes for the SP image readout is illustrated in Figure 1. The latent image signals is generated within a few microns from where the X-ray photon interact with the screen material. Therefore, there is minimal loss of spatial resolution in this process. However, the laser beam has a finite size which may be characterized by an intensity distribution at entrance surface of the screen. In addition, the laser beam is subject to photon scattering and light diffusion once it enters the screen^{5,6}. Both facts result in in a degradation of the spatial resolution quality⁸⁻¹¹. Although the propagation of the laser beam inside the screen, the excitation of the trapped electrons and release of their energy are rather complicated phenomena, the blurring process can be described by a simple model. In this model, the laser beam profile and light diffusion in the screen are characterized by the point spread functions (PSF's), PSF_B and PSF_S . The blurring process may be expressed as follows:

$$\begin{aligned} S(x, y) &= k \iint dx'' dy'' \sigma(x'', y'') \iint dx' dy' PSF_S(x''-x', y''-y') I_B(x'-x, y'-y) \\ &= kP_0 \iint dx'' dy'' \sigma(x'', y'') \iint dx' dy' PSF_S(x''-x', y''-y') PSF_B(x'-x, y'-y) \end{aligned}$$

where

$$PSF_B(x, y) = \frac{I_B(x, y)}{\iint dx' dy' I_B(r')} = \frac{I_B(x, y)}{P_0},$$

$I_B(x'-x, y'-y)$ = laser beam intensity profile at (x, y) in the detector plane,

$PSF_S(x''-x', y''-y')$ = point spread function for laser light diffusion at (x', y') ,

$\sigma(x'', y'')$ = area density of trapped electron energy.

$\sigma(x'', y'')$ and $S(x, y)$ may be viewed as input and output images respectively.

The above equations may be alternatively rewritten as follows

$$\begin{aligned} S &= kP_0 \cdot PSF_B \otimes (PSF_S \otimes \sigma) \\ &= kP_0 \cdot PSF \otimes \sigma \end{aligned}$$

and the pre-digitization point spread function, PSF , is formed from PSF_B and PSF_S as follows:

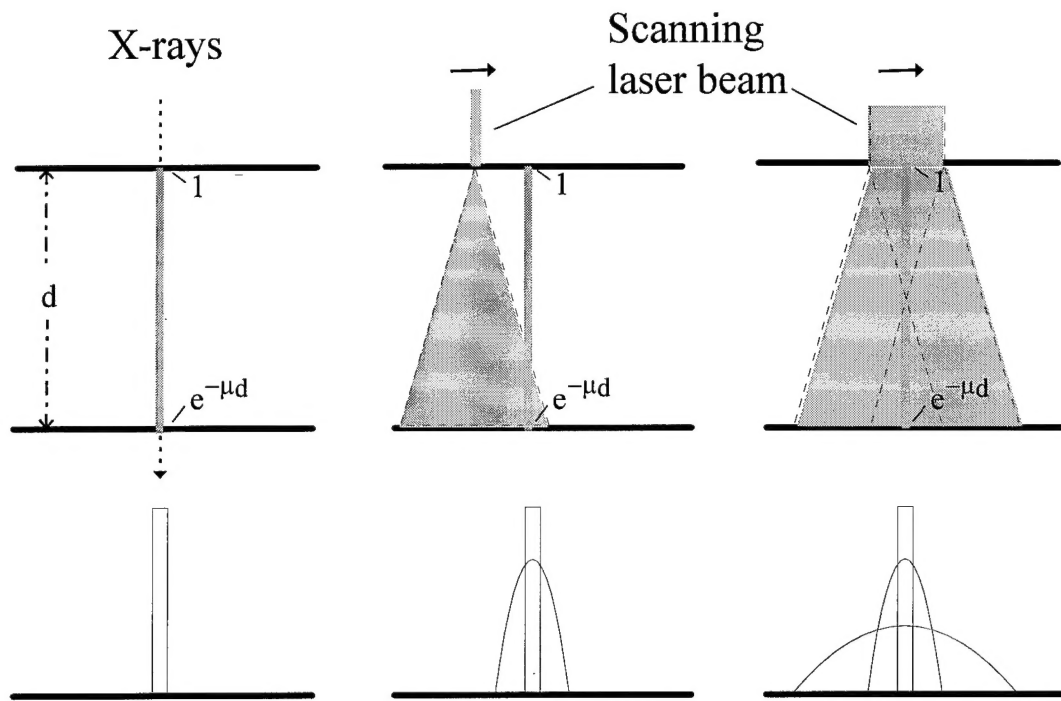


Figure 1 Schematic drawing for the image blurring processes in CR imaging

$$PSF = PSF_B \otimes PSF_S$$

PSF , PSF_B and PSF_S may be used to compute the line spread functions (LSF's) and MTF's. The resulting pre-digitization MTF, MTF , is related to the beam profile and screen MTF's, MTF_B and MTF_S , as follows:

$$MTF = MTF_B \otimes MTF_S$$

From the above equation, it is clear that both the beam profile and screen MTF's are important in determining the overall MTF or the spatial resolution quality of the imaging system. A large beam size or poor screen MTF or both would all degrade the resolution quality of the imaging system.

To estimate the effect of the beam spot size on the MTF, we may assume that the beam profile, $I_B(r)$, is a Gaussian function, with the full half maximum width, $d_{\frac{1}{2}}$. Based on this assumption, the point spread function, line spread function and MTF can be derived to be as follows:

$$PSF_B(x, y) = \frac{I_B(r)}{P_0} = \frac{4 \ln 2}{\pi d_{\frac{1}{2}}^2} \cdot e^{-4 \ln 2 \cdot \frac{r^2}{d_{\frac{1}{2}}^2}}$$

$$\begin{aligned} LSF_B(x, y) &= \int dy PSF_B(x, y) \\ &= \frac{2\sqrt{\ln 2}}{\sqrt{\pi} d_{\frac{1}{2}}} \cdot e^{-4 \ln 2 \cdot \frac{x^2}{d_{\frac{1}{2}}^2}} \\ MTF_B(f) &= e^{-\frac{\pi^2}{4 \ln 2} \cdot d_{\frac{1}{2}}^2 f^2} \end{aligned}$$

Using the above equation, the beam profile MTF is computed and plotted as a function of the spatial frequency for various beam sizes ($d_{\frac{1}{2}} = 22, 43, 65$ and $86 \mu\text{m}$) in Figure 2. At 2, 5 and 10 cycles/mm, the beam profile MTF values for a beam size of $43 \mu\text{m}$ are 97.4, 84.8 and 51.8% respectively. This means that with a beam spot size of $43 \mu\text{m}$, only slightly over 50% of the screen MTF at 10 cycles/mm is preserved in the overall MTF while those at 2 and 5 cycles are mostly preserved. A switch to $22 \mu\text{m}$ spot size would increase the MTF at 10 cycles/mm to 84.8% and preserve most of the screen MTF in the overall MTF at frequencies of up to 10 cycles/mm. On the other hand, an increase of the

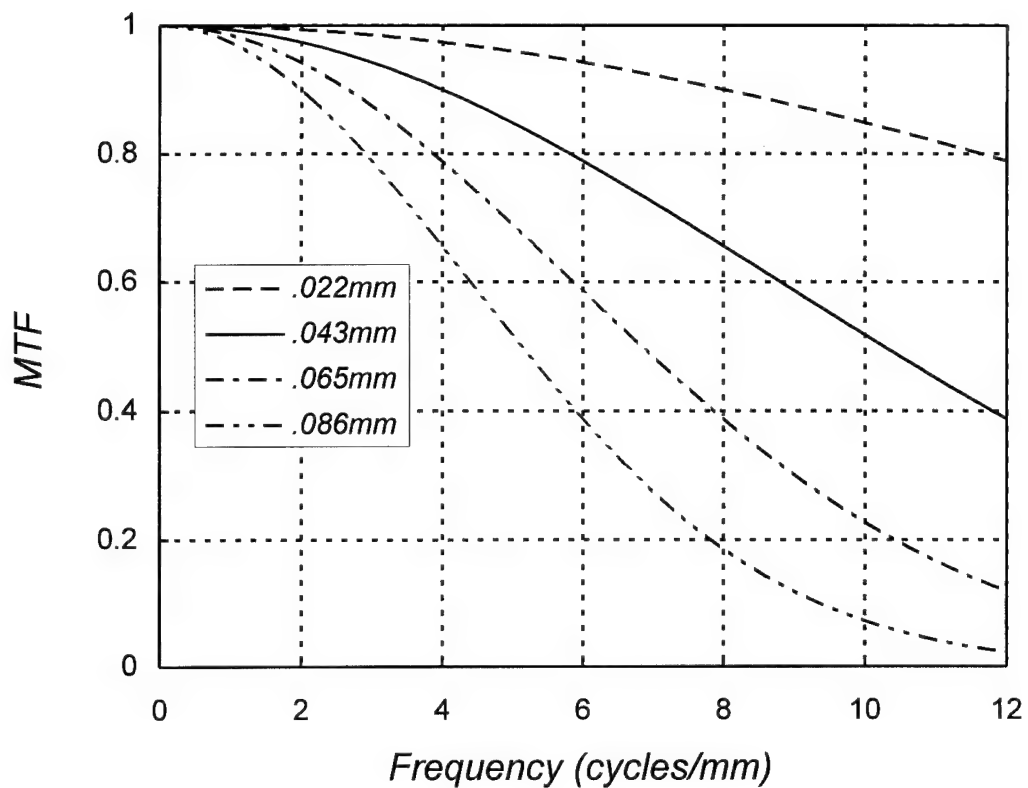


Figure 2 MTF's computed for four different laser beam spot sizes (half maximum width = 0.022, 0.043, 0.065 and 0.086 mm) for frequencies of up to 12 cycles/mm. The beam profiles are assumed to have the shape of Gaussian functions.

beam spot size to 86 μm would decrease the beam profile MTF to 7.2%. Combined with an already low screen MTF, this would reduce the overall MTF to almost zero level.

System Modifications

Figure 3 shows a schematic diagram of the laser scanning optics used in our experimental image reader. The collimated beam from an argon laser unit passes through a lens A and focuses at the acoustic optical modulator (AOM). The divergent output is collimated again by lens C, reflected by mirror D and focused again by a microscopic objective lens F. An aperture E is used to block the zero order peak and select the first order peak of the AOM output. The latter has an intensity adjustable through digital control of the AOM. The output of the lens F is collimated into a widened beam by lens G (beam expander) which is reflected by the mirror H and deflected by the digitally controlled galvanometer mirror I. The deflected beam passes through an F-theta or laser scan lens J and focuses on the image plane K.

The laser spot size at the image plane K, d, is determined by many factors including the focal lengths of the lenses A, E and J. The diameter of the expanded beam at the output of the lens G and the size of the galvanometer mirror I also pose limit on how small the laser spot size can be. In 1993, we successfully reduced the laser spot size from 120 μm to 50 μm by changing the focal length of lens A from 250mm to 125mm and replacing Lens F (previously a 5x microscopic objective lens) with a 10x one. As discussed before, the $1/e^2$ diameter, σ , is often used to describe the beam size in laser optics. σ can be estimated from d as follows:

$$\sigma = \sqrt{\frac{2}{\ln 2}} \cdot d$$

Thus, the $1/e^2$ diameter was reduced from 204 μm to approximately 85 μm .

To further reduce the beam spot size, we also replaced the AOM(Acoustic-Optical Modulator) with a more efficient one and move it to between the laser unit and Lens A. This is possible because the new AOM does not required focused beam and can operate on direct output from the laser unit. A small aperture (10-30 μm in diameter) will be positioned at the focal point between Lens A and Lens C. The use of this aperture will force the beam spot size to be reduced throughout the rest of the optics. However, a significant amount of laser power will be sacrificed through blocking the light outside the aperture.

Another source for loss of laser power is through the beam expander G, galvanometer mirror I and laser scan lens J. During our first stage of system modification, adequate but marginal laser power was achieved with currently used beam expander, galvanometer mirror and laser scan lens. However, they could limit the laser power to unusable range if further reduction of the beam spot size (down to 25-30 μm) is

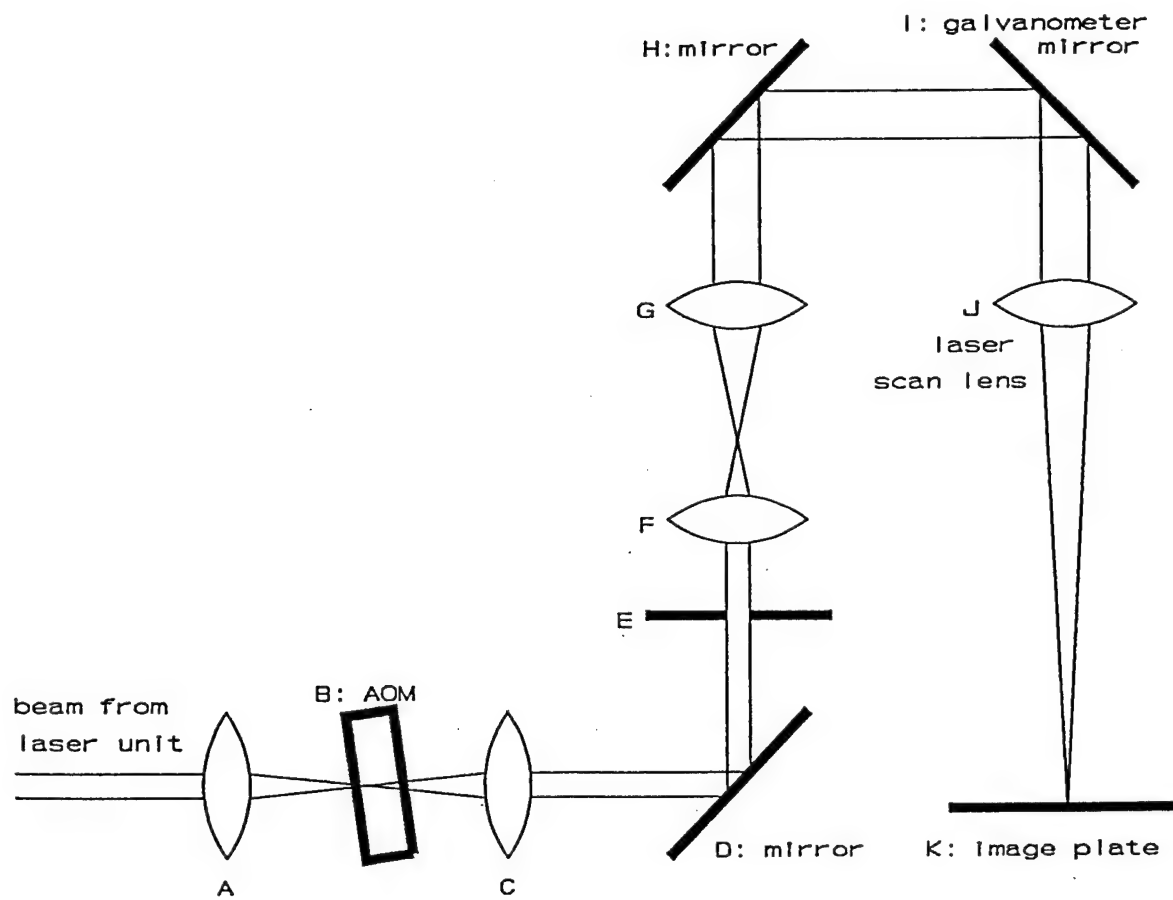


Figure 3 Schematic drawing for the laser scanning optics in an experimental CR image reader.

desired. Instead of replacing these components, a easier approach is to use a more efficient AOM (Multiwavelength Visible Light Modulator, Model No. N48062-2.5-.55, NEOS Technologies Inc.) and increase the power available at the beginning. The new AOM has a maximum light transmission of over 90% and therefore can produce a much higher power than the previously used one (made by Newport Research Inc., with an efficiency of less than 10%). This higher power provides us a greater flexibility in further reducing the beam spot size.

We also acquired a number of high resolution storage phosphor screens for use in image acquisition for the ROC studies. These screens include the newest one from Fuji: HR-V. However, our test showed that HR-V offers a spatial resolution quality similar to those of the HRIII series although it does produce a higher light gain.

Measurement of laser beam spot size

As discussed in the Theory section, laser beam spot size is one of the major factors that dictate the spatial resolution quality of the resulting CR images. To evaluate the laser spot size, two optical slit-photo Detector assemblies were constructed and attached to one end of the image plate carrier stage. Each assembly consists of a $5\mu\text{m}$ optical slit and a 2.5mm slit mounted in front of a photo-transistor (Figure 4). The photo transistor output is amplified and then forwarded to an oscilloscope for monitoring. It can also be digitized for analysis in the computer. However, a dedicated high speed analog-to-digital converter would be required to measure sub-millimeter spot sizes with reasonable precision. This option is being planned but not implemented yet.

To measure the laser beam spot size, the assemblies were first positioned in the laser scanning path. As the laser beam scanned across the two optical slits in each assembly, a signal consisting of two pulses was generated (Figure 5). This signal is proportional to the laser beam power profile, integrated in the longitudinal direction (in which the translational stage moves). The slit signal can be observed on a scope to measure the full width at half-maximum of the two pulses. Assuming the (half maximum) pulse widths for the $5\mu\text{m}$ and 2.5mm slits are t and T respectively, the half maximum width of the laser beam profile on the image plane, d , can be estimated as follows:

$$d = 2.5\text{mm} \times \left(\frac{t}{T} \right)$$

The process of measuring the laser beam spot size was later automated. Instead of being displayed on a scope, the slit signal is digitized and analyzed in a microcomputer to provide both the half-maximum and e^{-2} widths. The measurement can be repeated at a rate of approximately 1 per second to allow the optics to be adjusted while monitoring the beam spot size. The difficulty with measuring the laser spot size resides with the location of the maximum and background levels. Errors in determining these levels may bias the

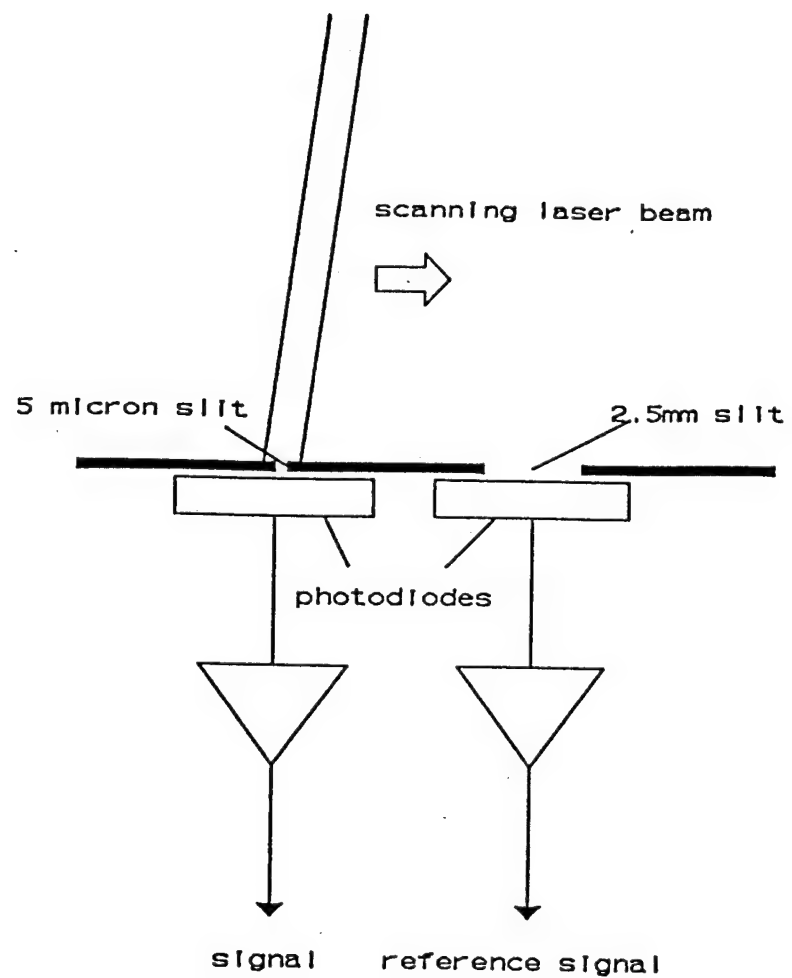


Figure 4 Experimental setup for measuring the laser beam spot size.

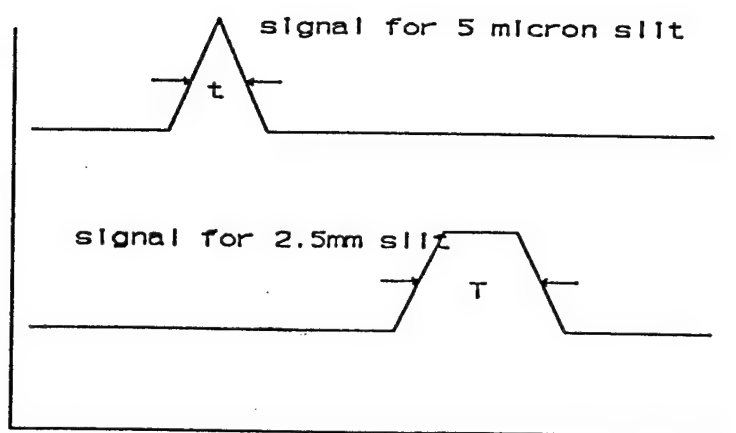


Figure 5 Phototransistor signal outputs for the $5\mu\text{m}$ and 2.5mm optical slits.

measurements. With continuing refinements, the smallest beam spot size we could have achieved was measured to be 30 μm for the FWHM or of 70 μm for e^{-2} width in the high resolution mode. This corresponds to a MTF value of approximately 70% at 10 cycles/mm.

Further reduction is possible. However, it may start to degrades the sampling process and generate gaps where x-ray information would be lost and image noise may increase. Although we continue to investigate the pros and cons of smaller spot size, we have reached the conclusion that based on practical considerations, it would be a good compromise to use 40 μm laser beam spot in our comparison study.

We have also developed a series of techniques for testing the operation of ESPIS. One of these techniques is direct measurement of the scanning laser intensity pattern. We have been able to use film to monitor and measure the spatial intensity distribution of the scanning laser beam. This technique has proved to be useful in checking the stability of the laser power or the proper function of the AOM.

System Configuration

The CR imaging system used in this study is an experimental system built on an optical bench with standard optics components and a high power argon laser unit. The system employs galvano-mirror to provide a scanning laser beam. During scan readout, the SP image plate is placed on a translational stage and moved into the scanning laser beam for signal readout. The system is capable of scanning and digitizing with a variety of pixel sizes, including the frequently used 172, 86 and 43 μm . The readout signals are digitized into 12 bit data without going through logarithmic amplification or mapping. An adjustable active bandpass filter system is used to match the bandpass frequency of the signal input to the analog-to-digital converter.

A LoRAD M-III mammographic unit was used to provide X-ray exposures. A variety of image plates are available for use with our SP system. For this study, Fuji HR IIIIn and ST IIIIn plates (cut to size of mammographic screens) were housed in Kodak Min-R cassettes for exposures. This unit employs molybdenum target and reciprocating grid. For screen-film images, Kodak Min-R screens are used in conjunction with Kodak Min-R E film.

SYSTEM CHARACTERIZATION

Modulation Transfer Function (MTF)

We continued to use a lead bar resolution pattern (Nuclear Associates 07-553) to monitor and measure the spatial resolution quality of the ESPIS. It consists of 22 groups of bar patterns with a frequency ranging from 0.25 to 10 lps/mm. Each group has a 4 cycle bar pattern. A specification list for the resolution bar pattern is attached as Appendix I.

The bar pattern images are visually examined to evaluate the spatial resolution limit of the imaging system. A fully resolved pattern (with good contrast) generally indicates that the MTF is around 0.05 or greater at that particular frequency. A partially or barely resolved pattern with faint contrast indicates that the MTF is probably between 1% and 5%. Unresolved bar patterns generally indicate that the MTF is below 1%. This observation could vary from person to person but may be used a crude guideline when visually examining the bar pattern images.

The methods for measuring the spatial resolution properties of a storage phosphor imaging system have been previously discussed and demonstrated^{8,9,12,13}. Our methods focus on the use a standard resolution test pattern as described before. The square wave response function (SWRF) can be measured by plotting the signal profile across the bar patterns and then measuring the average amplitude for each frequency. Because the square waves contain high order harmonics, the SWRF can not be directly used to compute the MTF without correction for these harmonics. We have devised and tested a signal processing method to compute the MTF from the signal profile of a bar pattern.

The MTF is measured from the digital SP images of a resolution bar pattern (Nuclear Associates 07-553) to evaluate the spatial resolution quality of the resulting images. This pattern provides bar patterns at frequencies ranging from 0.25 to 10 cycles/mm. To measure the MTF, the image of the bar patterns is first segmented into sections of various frequencies. Signal profiles across the bar patterns from each section are then concatenated over 20 lines into a long array of signals modulated at a single frequency. This array is offset to correct for x-ray transmission through lead bars and the presence of scatter signals. The Fourier transform of this long array is then computed to and used to obtain a frequency spectrum of the signals. This spectrum contains a primary peak, corresponding to the frequency of bar patterns, and higher order harmonics at multiples of this frequency. These harmonics are ignored in the computation of the MTF. The height of the primary peak, $S(f)$, is normalized by the DC component, $S(0)$, to compute the MTF at the frequency at f as follows:

$$MTF = \frac{S(f)}{0.6369 \cdot S(0)}$$

where the correction factor 0.6369 is the height of the primary peak, normalized by the DC component, in a perfect square wave, toggling between 0 and some positive value. This method provides an rather easy way to evaluate the MTF or spatial resolution properties of a digital imaging system.

We have measured and compared the system MTF's for two different laser beam spot sizes: 30 and 50 μm (FWHM). The results, shown in Figure 6, indicate a significant improvement of the MTF. Notice that the ratio of improvement is rather insignificant at low frequencies. However, it becomes more and more significant as the frequency increases. The MTF value almost doubles at frequencies above 6 cycles/mm. Despite the improvement, the MTF values are still low at high frequencies. Further increase of the MTF would require a significant improvement of the CR screens.

We have also measured the MTF as a function of the laser beam power, ranging from 8 to 12 mW. The results, shown in Figure 7, indicate that the MTF does not depend on the laser beam power in the useful range of 8-12 mW. It should be noted that outside this range, the power may be too strong to avoid overheating or even burning the phosphor or too low for the position encoding to properly function.

In Figure 8, the MTF is plotted as a function of the frequency for both the HR and ST screens to demonstrate the improvement from using a HR screen. The MTF with the HR screen is generally higher at all frequencies except at very low (near 0.25 cycles/mm) and very high frequency (near 10 cycles/mm). The closeness of the HR and ST MTF values near 10 cycles/mm is rather puzzling. However, it may be partially explained by the fact that in mammographic imaging more X-rays are absorbed near the screen surface (assuming that X-rays enter the screen from the surface) and high frequency signals may be mostly generated near the screen surface.

In Figure 9, the MTF of our high resolution CR system is compared with a typical commercial system operated in two different techniques (an early KESPR prototype by Eastman Kodak Company). One technique employs 172 μm pixel size to generate 2048 x 2500 images for 14"x17" field size. This is configured for medium resolution applications like chest imaging. A second typical technique employs 100 μm pixel size to generate 2048 x 2500 images for the smaller 8"x10" field of view. This configuration provides slightly better resolution and is intended for more demanding applications like pediatric or orthopedic imaging. Figure 9 shows that our high resolution CR system produces significantly better MTF than either techniques with the commercial system. Because similar CR screens were used (ST for 14"x17" and HR for 8"x10"), the lower MTF's of the two commercial techniques are probably due to the larger spot size used. The larger pixel sizes used by the commercial systems may also contribute to the degradation of the MTF's.

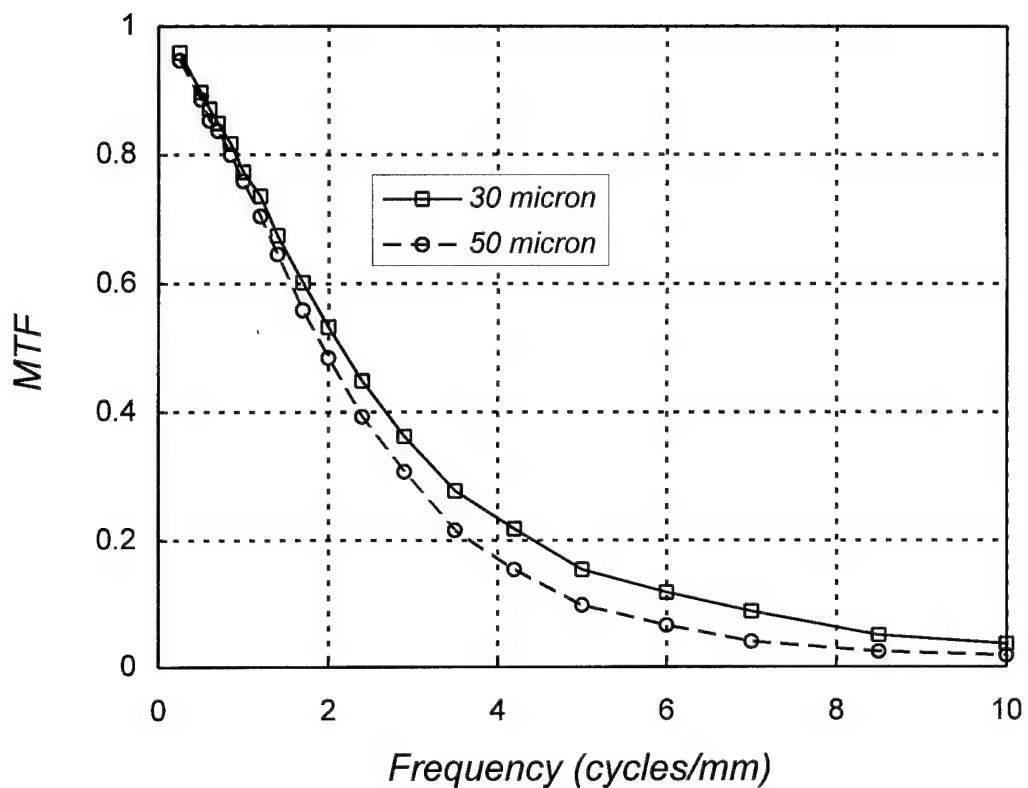


Figure 6 MTF's of a CR imaging system: 30 μ m versus 50 μ m laser beam spot sizes.

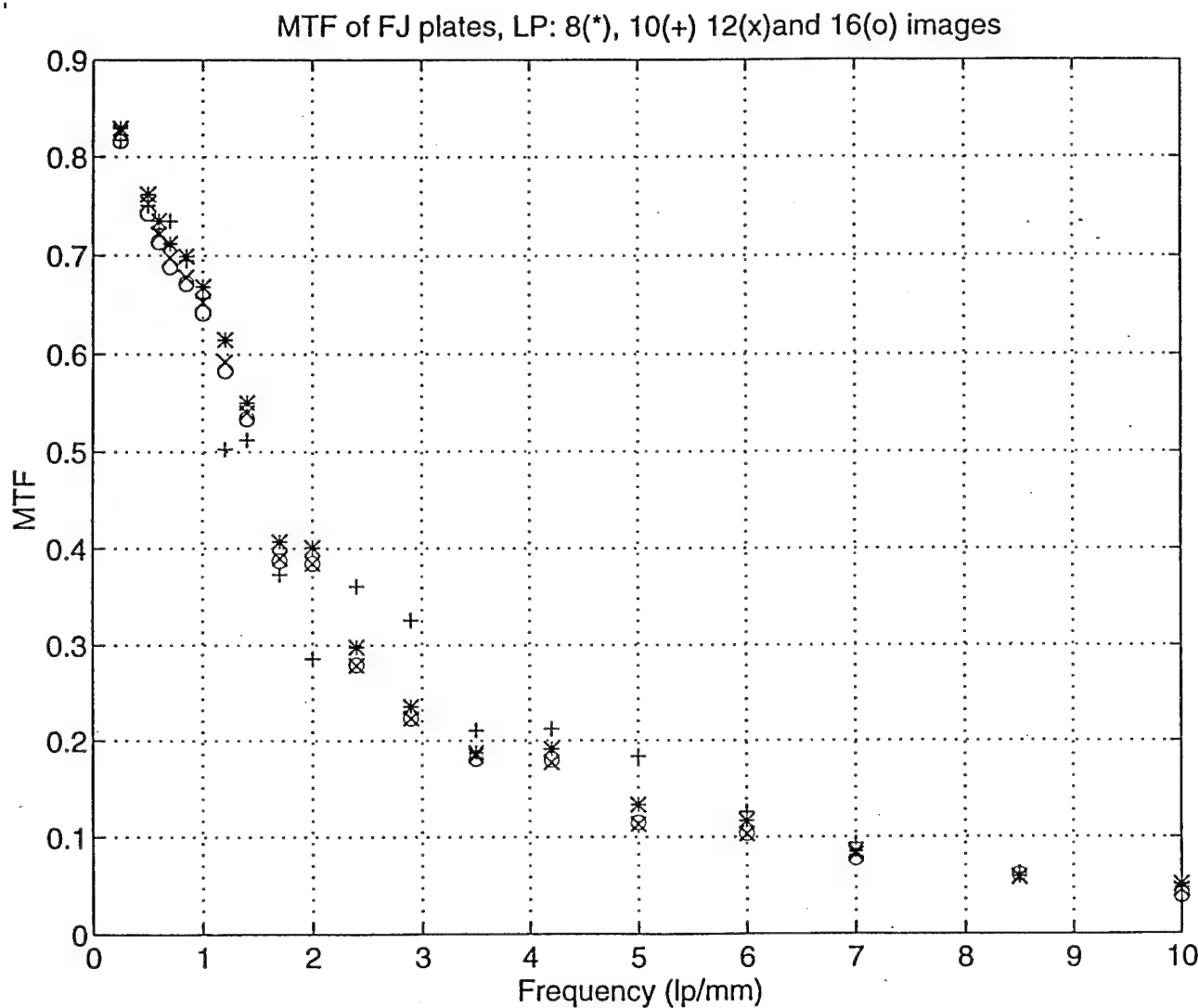


Figure 7 Effect of laser power on the MTF. The MTF was measured for various laser powers, ranging from 8 to 16 mW: "*": 8 mW, "+": 10 mW, "x": 12 mW and "o": 16 mW.

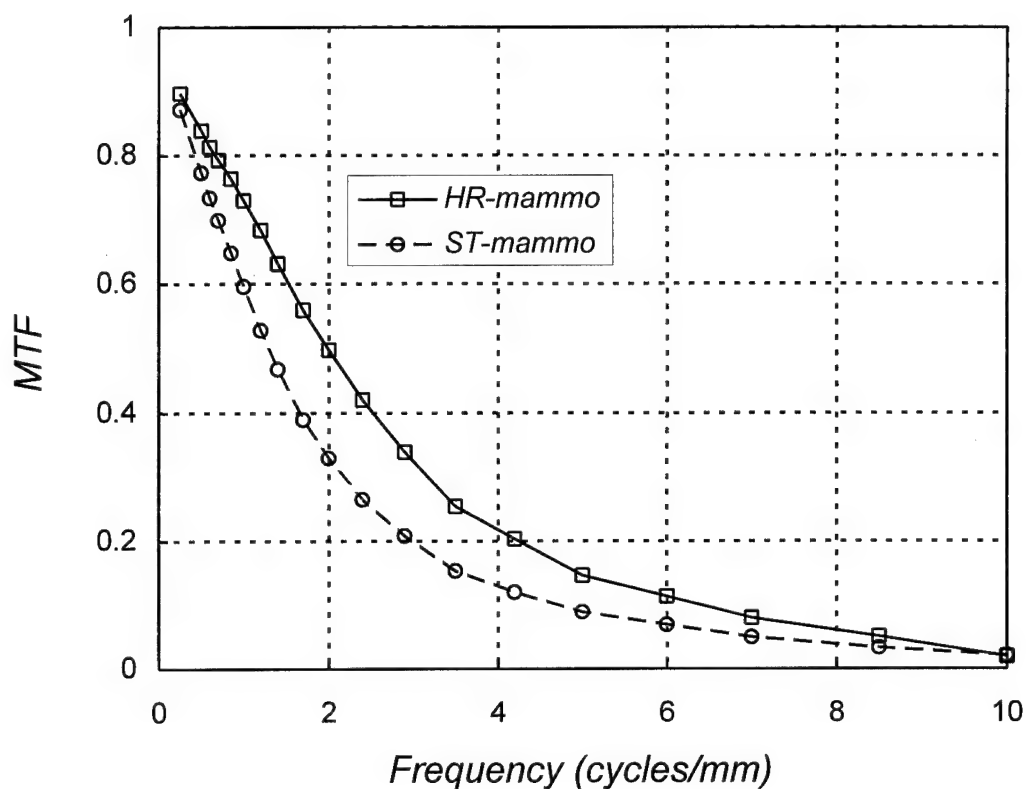


Figure 8 MTF of the high resolution CR imaging system: HR screen versus ST screen.

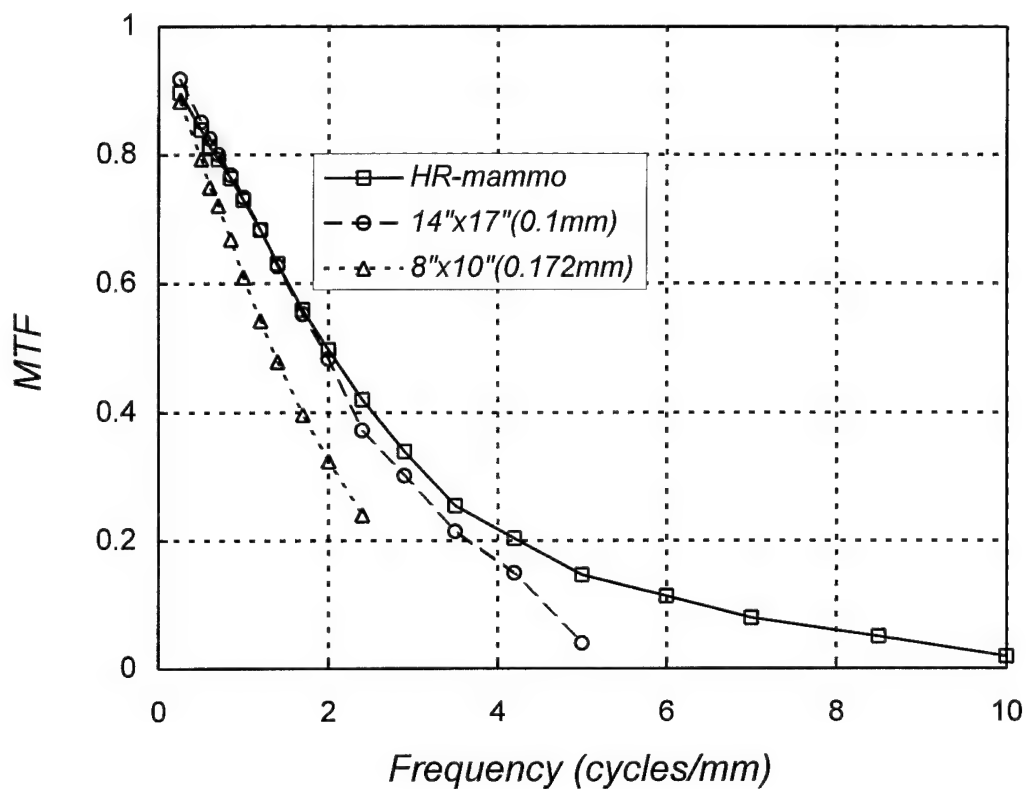


Figure 9 MTF's of CR imaging systems: our high resolution CR imaging system versus typical commercial systems.

In Figure 10, the MTF of our high resolution CR system measured with a mammographic exposure (25 kVp, 10 mAs) is compared with that measured with a typical chest exposure (110 kVp, 6 mAs). The plots show that the MTF is significantly higher with mammographic exposures. This may be explained by the fact that high frequency signals are mostly generated near the surface of the screen and the latent image signals are distributed more toward the screen surface with the mammographic X-rays than with chest X-rays. MTF's measured with high kVp mammographic exposures should be between the two MTF's shown in Figure 10.

Films 1 shows a screen-film image of a resolution test pattern (Nuclear Associates, Model 07-553) acquired with a mammographic unit at 25 kVp and 6 mAs. Films 2, 3 and 4 show CR images of the same pattern acquired with three different techniques: (Film 2) exposed with a ST screen and read out with 30 μm laser beam size, (Film 3) exposed with a HR screen and read out with 30 μm laser beam size and (Film 4) exposed with a HR screen and read out with 50 μm laser beam size. All images were read out with a pixel size of 43 μm . Notice that the screen-film image displays best resolution: all bar patterns are clearly resolved. The image in Film 3, acquired with HR screen and small beam spot size, shows the best spatial resolution quality among the three CR images. Large beam spot size, thicker ST screen or both degrade the spatial resolution quality of the imaging system.

Detective Quantum Efficiency

Detective quantum efficiency (DQE) is often measured as a function of the spatial frequency and used to characterize the capability of an imaging system to preserve the signal-to-noise ratio (SNR) in the input image signals. DQE is generally defined as follows:

$$DQE = \frac{SNR_{out}^2}{SNR_{in}^2}$$

where SNR_{in} and SNR_{out} are the image signal-to-noise ratios at the input and output. To measure the DQE as a function of the spatial frequency, f (lps/mm), we used the following expression for the frequency dependent DQE:

$$DQE(f) = \left(\frac{1}{SNR_{in}^2} \right) \cdot \left(\frac{S^2}{NPS(f)} \right) \cdot MTF(f)^2$$

where $NPS(f)$ is the noise power spectrum, S is the average signal over the area where $NPS(f)$ is measured, $MTF(f)$ is the modulation transfer function. This equation is similar to those previously used in literature on DQE measurement^{8,9,11,15}.

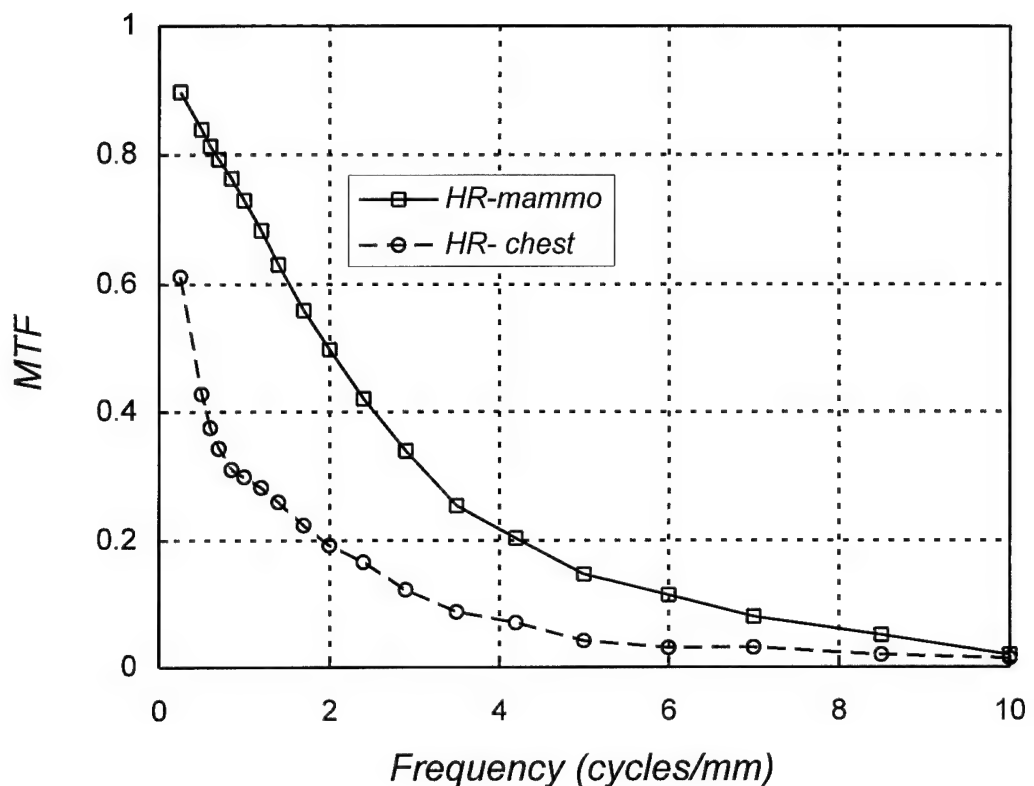


Figure 10 MTF's of the high resolution SP imaging system: mammographic technique versus chest imaging technique.

We have measured the noise power spectrum (NPS) and detective quantum efficiency (DQE) for our CR system. To compute the DQE(f), NPS(f) is computed from image data over an area with largely uniform signals while SNR_m is computed from the number of photons which is estimated from the x-ray techniques used. Figure 11 shows the noise power spectrum computed from the image data in a largely uniform region. The x-ray techniques used in acquiring the image data are 25 kVp, 10 mAs, with grids at an SID of 65 cm. The resulting detector exposure is approximately 6 mR. Notice that because of image blurring, the noise spectrum is no longer white. Instead, it decreases with increasing frequency. Figure 12 shows the DQE plotted as a function of the frequency.

The reduction of laser beam spot size affects the DQE mainly through the MTF improvement. However, if the laser beam size is too small as compared to the pixel size, loss of quantum detection efficiency may occur and degrade the DQE at all frequencies.

Quality Control

Quality control of the CR imaging system has been performed by acquiring and visually checking images of the resolution bar pattern, CIRS phantom, RMI phantom and the specially designed aluminum wire phantom. Because some improvements have been made on the system, the criteria for visual check has slightly changed now. In general, for the resolution bar pattern image, we expect to see and resolve all bars at frequencies of up to 8.5 lps/mm fully and clearly. The 10 lps/mm bars should also be fully resolved but with subdued contrast. Partially resolution of the 10 lps/mm bars is an indication of presence of structural artifacts. The images of the CIRS phantom provides a convenient semi-quantitative method for checking the overall quality of the system, including the spatial resolution and noise properties. Same technique (25kVp, 144mAs, 65cm SID, with antiscatter grids) will be used in all quality control exposures. In general, we expect to see all microcalcifications with a diameter of 200 μ m or greater and all masses with a diameter of 2mm or greater. All fibrils should be fully resolved. The RMI phantom offers a more qualitative check. All images should have similar apparent quality as previous images. The aluminum wire phantom provides a finer technique to grade the system performance. At 25 kVp and 26 mAs, we expect to resolve the 1" long wires as thin as 50 μ m in diameter and small wire segments as thin as 125 μ m.

Quality control of mammographic X-ray units and the screen-film combinations have been previously discussed^{110,111}. The quality of the mammographic X-ray unit is routinely monitored and maintained by the clinical staff.

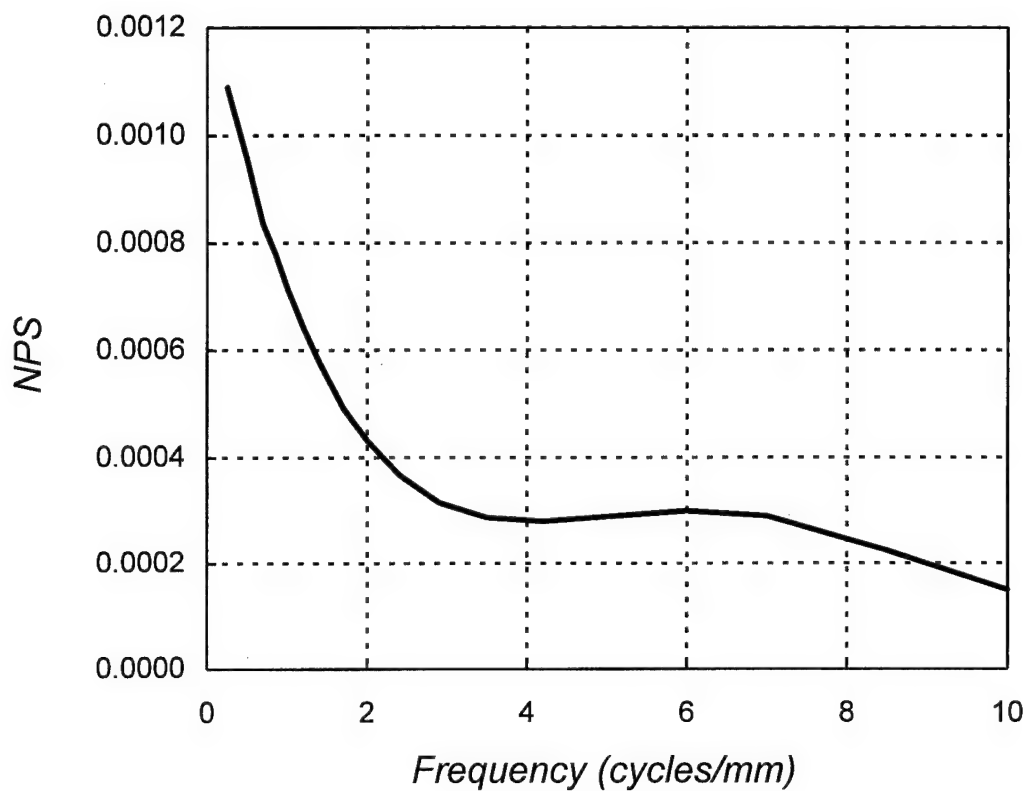


Figure 11 Noise power spectrum (NPS) computed from image data in an area of largely uniform brightness. The spectrum was normalized by dividing it by the square of the average signal.

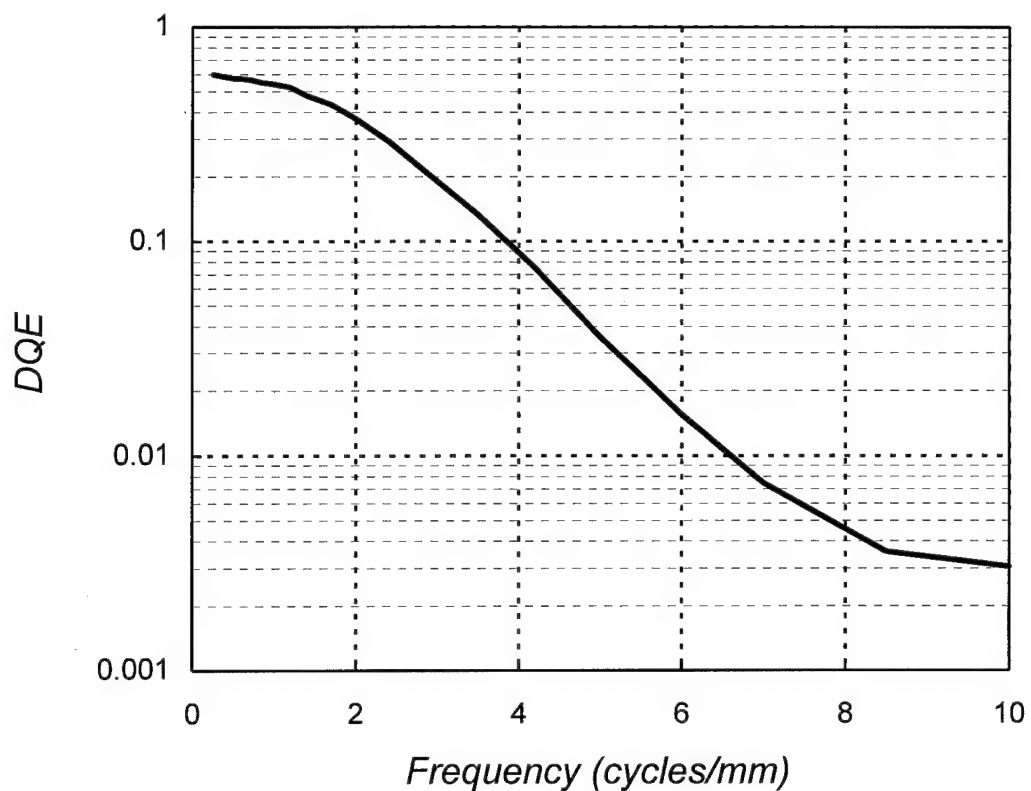


Figure 12 DQE versus spatial frequency for the improved experimental CR imaging system.

COMPARISON- PHANTOM IMAGES

Phantom Selection and Design

Image quality of a mammographic unit is often checked with phantoms simulating a breast with the three major disease symptoms: microcalcifications and masses. Various phantoms have been designed for this purpose. We have used two commercial phantoms to test the image quality and compare different imaging systems or technical factors. The first one is a Tissue-Equivalent Breast Phantom made by the Computerized Imaging Reference Systems (CIRS), Inc. of Norfolk, Virginia. It consists of a breast shape phantom made of tissue equivalent material, with a step wedge, groups of microcalcifications, masses and fibrils embedded inside the phantom. A specification sheet for the phantom is attached as Appendix II. The step wedge consists a square region with a contrast corresponding to additional 5mm of glandular tissue over the surrounding background tissue and a second square region with a contrast corresponding to additional 5mm of fat tissue. The 12 microcalcification groups ranges from 0.12mm to 0.35mm in diameter. The 6 masses range from 1mm to 6mm in diameter. The fibrils have a diameter of $8.7\mu\text{m}$. This phantom provides a good tool for comparing the overall image quality of different imaging systems, techniques or technical factors.

The second phantom is the RMI Anthropomorphic Breast Phantom (Model 165, Gammex-RMI). The phantom consists of a breast tissue equivalent (50% adipose, 50% glandular) plastic casting and a high resolution detail layer enclosed in a protective acrylic case. Together, these components produce radiographic images that are similar to a true mammogram.. To aid the evaluation of system performance, the phantom also produces a nine level gray scale step wedge and a group of resolution line pairs in the mammogram. The phantom is unique in that the characteristics of its components were derived from an actual mammogram. The three dimensional surface structure of the breast tissue equivalent plastic casting produces the low and medium resolution image detail. High resolution image details are produced by an attenuating coating of a stable mercury-silver amalgam on photographic film. In addition to protecting the contents, the acrylic case acts as a uniform attenuation layer across the entire phantom

The advantage of using the above two phantoms is that they more or less resemble a real breast in tissue thickness, composition and even structures. Thus they allow the performance to be checked in a realistic fashion. However, they are more suitable for quality control than for critical comparison of image quality. The simulated microcalcifications in the CIRS phantom have a size of at least $120\mu\text{m}$. In addition, the sizes of different groups increment by $40\mu\text{m}$. To facilitate more critical and quantitative comparison of image quality, we have developed a phantom referred to as the perception phantom. The perception phantom was constructed of aluminum wires of 8 different sizes: 2, 3, 4, 5, 6, 7, 8 and 16 mils. These wires were cut into about 1" long and placed in radial directions over a 1" thick Lucite block. A group of five short wire segments, cut from the same size of wire, are placed near the tip of each wire. These groups of short

wire segments are intended for simulating microcalcifications. They were also placed in overlap with the anthropomorphic phantom to simulate microcalcifications in the breast. This phantom allows subtle difference between different imaging systems or techniques to be detected.

Image Acquisition

The three phantoms were first imaged with a conventional screen-film combination (Kodak Min-R screen-film combination) in the photo-timed mode. After ensuring that the resulting film has adequate density, a cassette containing a CR screen was exposed with exactly the same technique. All images were taken at 25 kVp with the reciprocating grid in place. The mAs used were 144, 22 and 104 for the tissue equivalent breast phantom, perception phantom and anthropomorphic breast phantom respectively. Two different types of CR screens, HR and ST, were used for exposure. The exposed screens were scanned in the high resolution mode using a pixel size of 43 μm and a laser beam spot size of 30 or 50 μm (full width at half-maximum).

Phantom Images

Films 5 shows a screen-film image of the perception phantom acquired with a mammographic unit at 25 kVp and 22 mAs. Films 6, 7 and 8 show CR images of the same phantom acquired with three different techniques: (Film 6) exposed with a ST screen and read out with 30 μm laser beam size, (Film 7) exposed with a HR screen and read out with 30 μm laser beam size and (Film 8) exposed with a HR screen and read out with 50 μm laser beam size. All images were acquired at 25 kVp and 22 mAs and read out with a pixel size of 43 μm .

The wires segments have a sharper appearance in the SF image. In the screen-film image (Film 5), the 5 mil or thicker (125 μm) wire segments are well resolved while the 4 mil (100 μm) wire segments are only marginally resolved. In the optimized CR image (Film 7), all wires with a thickness of 5 mil or thicker are resolved. The long wires are easier to see. All but the 2 mil (50 μm) long wires (oriented in radial direction) are resolved. The screen-film image shows the wire segments with a sharper appearance which is partially due to its smaller (by a factor of 2) format. This helps resolve the 4 mil (100 μm) wire segments. However, it does not resolve finer segments (2, 3 mil) or wires (2 mil). This shows that at typical clinical exposure level (as determined by the automatic exposure control), the improved storage phosphor imaging system approaches the conventional screen-film combinations in quality as far as detection of microcalcifications is concerned. The use of larger beam spot size or thicker screen does not seem to affect the detection of the 5 mil or thicker wires in the CR images.

Films 9 shows a screen-film image of the tissue equivalent breast phantom acquired with a mammographic unit at 25 kVp and 144 mAs. Films 10, 11 and 12 show CR images of the same phantom acquired with three different techniques: (Film 2)

exposed with a ST screen and read out with 30 μm laser beam size, (Film 3) exposed with a HR screen and read out with 30 μm laser beam size and (Film 4) exposed with a HR screen and read out with 50 μm laser beam size. All images were acquired at 25 kVp and 144 mAs and read out with a pixel size of 43 μm .

Probably because of their spherical shape, the simulated microcalcifications in the tissue equivalent breast phantom are more difficult to detect than the aluminum wire segments in the perception phantom. Both SF and CR images can resolve 200 μm microcalcifications. Neither can resolve the 160 μm microcalcifications. Because the CR image can be enhanced for better display contrast, the SP image actually shows the circular simulated masses better than the screen-film image. However, it doesn't resolve smaller masses than the screen-film image. The screen-film image shows the calcifications, masses and fabrils with a sharper appearance which is partially due to its smaller (by a factor of 2) format. However, it does not resolve more microcalcifications than what can be resolved in the CR image. It seems that the size differences of the simulated microcalcifications and masses in this phantom are too coarse to differentiate the performance differences between the SF and various CR techniques.

Films 13 shows a screen-film image of an anthropomorphic breast phantom acquired with a mammographic unit at 25 kVp and 104 mAs. Films 2, 3 and 4 show CR images of the same phantom acquired with three different techniques: (Film 14) exposed with a ST screen and read out with 30 μm laser beam size, (Film 15) exposed with a HR screen and read out with 30 μm laser beam size and (Film 16) exposed with a HR screen and read out with 50 μm laser beam size. All images were acquired at 25 kVp and 104 mAs and read out with a pixel size of 43 μm .

With the SF image, 5 mil or thicker wires can be detected while with the best CR image (Film 15) only 6 mil and thicker wires can be detected. Notice that with the CIRS breast phantom or the perception phantom, the contrast objects are detected over uniform background and the SP and SF are comparable to each other in performance. The sharper appearance of the SF image has an advantage here probably because the sharper appearance of the SF image help differentiate the simulated microcalcifications from the overlying background structures. The use of thicker screen or larger beam spot size result in more blurred look of the images, making it slightly more difficult to see the simulated microcalcifications.

There are several lessons learned from this comparison study based on visual comparison of the phantom images. First of all, commercial phantoms are inadequate for comparing the CR with the SF techniques. The problems seem to reside on the fact that the size differences in the simulated microcalcifications and masses are too coarse to be used to depict any subtle difference in performance. The use of aluminum wire segments with a range of closely spaced sizes help depict the difference. However, a far better comparison technique should be the use of ROC studies.

COMPARISON STUDY- ROC STUDIES

The ROC studies provide a means to quantitatively compare two imaging techniques. Two ROC studies were conducted to compare the improved CR imaging technique with the conventional screen-film technique. The studies were based on phantom images with simulated microcalcifications and masses. To present more realistic imaging conditions, these objects were superimposed with structures mimicking tissue structures of breasts. Methods and results for these are described and discussed in the following sections.

Phantom Design

The main body of the phantom is supposed to provide a background structure over which microcalcifications and masses will be simulated and superimposed. We have investigated several approaches to construct the main body of the phantom. The final design is a large 1" thick piece of beef housed in a specifically designed plastic tank. This design is intended to simulate a well compressed breast. The meat produces a structural pattern different from real mammograms but still provides adequate challenge to the tasks of detecting simulated microcalcifications or masses. The meat can be easily replaced to produce a different structural background so that the reader has no opportunity to become "trained" for a certain pattern. The tank is filled with pure alcohol to preserve the meat for longer time. The thickness of the tank is minimized to about 0.5". Thus, the phantom has a total thickness of 1.5".

Mircocalcifications (MC) are simulated by a group of 5 or 6 aluminum wire segments (spread over an area of 2-3 mm wide) placed on a 1.5"x1.5" piece of plastic film (cut from acetone transparency). The MCs are simulated with two different sizes: 5 or 6 mils(125 or 150 μ m). Other sizes weren't used because visual tests have indicated that MCs larger than 6 mil are too easy to see while those smaller than 5 mil can never be seen when overlapping with some tissue structures. For each size, many film inserts were made with the MCs located at various locations. These films can also be rotated by multiples of 90 degrees to further randomize the location of the MC groups. Films without any MC were also made to simulate normal cases. A film holder is constructed of a 3/8" thick piece of Lucite with a 3x4 matrix of 1.5"x1.5" holes cut out.. During image acquisition, the holder, with 12 selected film inserts, is placed underneath the meat phantom for exposure. Figure 13 shows the layout of these cutouts. Films 17 and 18 show a CR and a screen-film image of the meat phantom with simulated MCs.

Statistical analysis in the proposal has indicated that 240 observations (readings) are required to yield reasonable significance of the ROC study. Our phantom design provides 12 "windows". Within each of these windows, an observation or reading can be performed to determine whether and where there are MCs. Thus, each image will provide 12 independent readings. In our studies, a total of 24 images were acquired, providing a total of 288 different detection tasks for each reader. 144 film inserts were

Trial No. 1

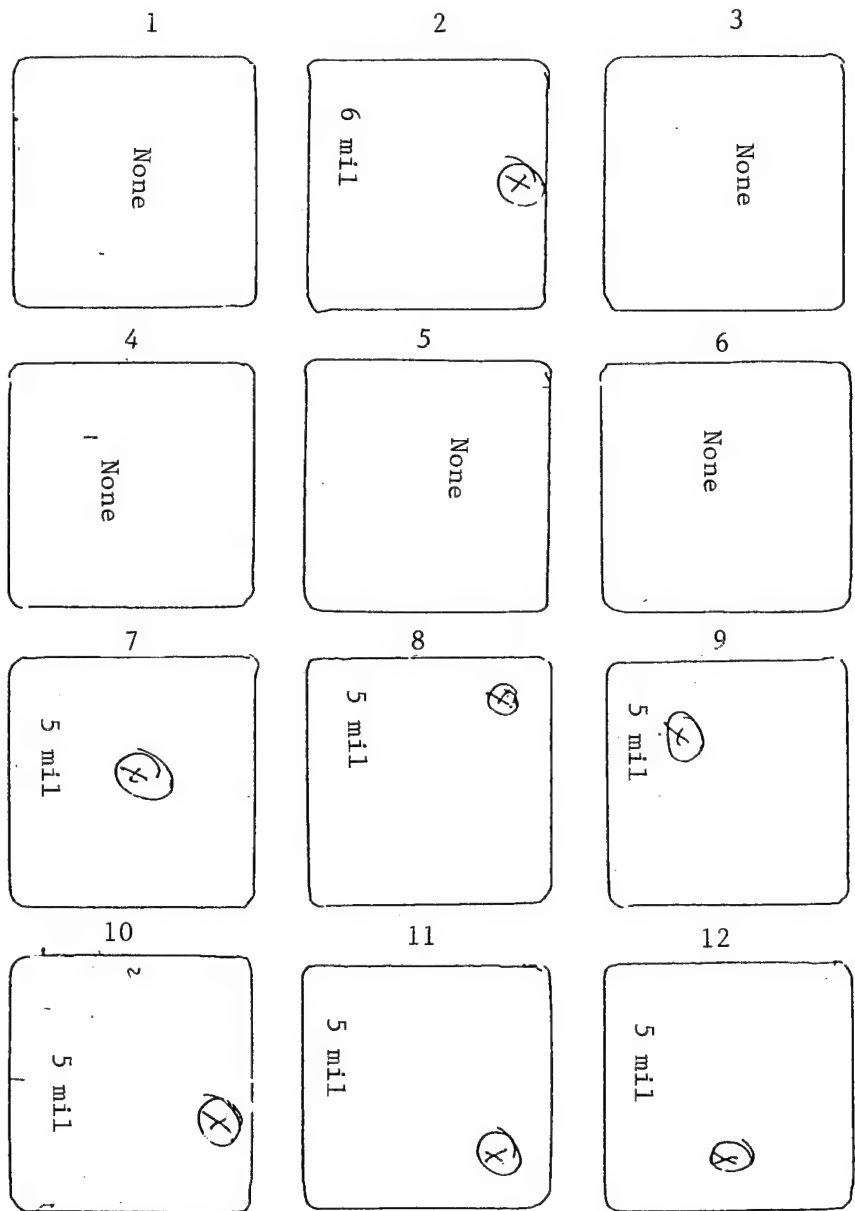


Figure 13 Layout of the film holder for the meat phantom used to acquire images for the ROC study. A matrix of 3x4 1.5" x 1.5" film inserts can be placed on the holder to provide 12 independent reading tasks. Examples of the microcalcification placement are shown in the windows #2,3,5,7,8,9,10,11,12.

generated without any microcalcifications and used as control. 72 film inserts were produced with 6 mil MC's. Another 72 film inserts were produced with 5 mil MC's. Using a computer program, these inserts were randomly selected and placed during the acquisition of each image.

The masses are simulated by a circular piece of film.. The edges of the film pieces were ground to obtain smooth border. The variation of the grinding procedure produces mass-like objects with variable and marginal visibility. A total of 24 images were acquired, each containing 3x4 1.5"x1.5" small regions for 12 independent detection tasks. Among a total of 288 image regions, half of them have no simulated mass and half of them have one mass placed at the center of the image or at center of one of the four quadrants. The distribution and placement of the massess in the images were randomized with the help of a computer program. Films 19 and 20 show a CR and a screen-film image of the meat phantom with simulated masses.

Image Acquisition

A clinical mammographic unit (LoRAD M-III) is used for image acquisition. The x-ray tube uses a molybdenum target. A 5:1 reciprocating antiscatter grid is used. With the phantom in place, a screen-film image is first taken using Kodak Min-R screen and Min-R E film in the autotimed mode. The kVp is kept fixed at 25 kVp and the mAs is controlled by photo-timing. Following the exposure, the mAs will be recorded. The exposed film will then be developed and checked for proper exposure. If the film exposure is adequate, the storage phosphor cassette will be inserted and exposed using identical x-ray techniques. The exposed storage phosphor screen will then be scanned with a pixel size of 43 μ m to generate a 4096x5000x12 bit digital image. The image will first be printed with a 80 μ m pixel size using a Kodak Ektascan laser printer. The film will be examined and checked for any artifacts or phantom position. If acceptable, the phantom will be fitted with a different set of film inserts and imaged again following the same procedure.

Data Collection

The CR images are printed with a pixel size of 50 micron to produce films of a size (8"x10") similar to that of mammograms (18cm x 24cm). Because we do not have a printer capable of printing with 50 μ m pixel size, the CR image data were sent to Eastman Kodak Company for printing. Within each ROC study, either microcalcification or mass detection study, a total of 24 x 12 = 288 sub-images are available for reading and scoring for each imaging technique. Five board certified mammographers were asked to read and score the 288 sub-images acquired with the CR technique and another 288 sub-images acquired with the SF technique.. A computer program was written to manage the reading study and to record the scores. The scores, ranging from 0 to 100, represent the confidency level for the microcalcifications or mass to be present. If a score of 50 or

higher was entered, the reader was also asked to enter the perceived location of the microcalcification group or mass. This location information was recorded along with the confidence levels for future analysis.

ROC Data Analysis

The results from the reading sessions were analyzed using the ROC software developed by Dr. Metz at the University of Chicago. Notice that in ROC analysis the location information is ignored. The location information will be used in the LROC analysis which would lower the scores if the locations entered are incorrect ones. It would be interesting to compare the LROC analysis with the ROC analysis to see if incorrect locations has any impact on the final outcome. In a small scale preliminary study, we have found that the locations entered by the readers are mostly correct ones and therefore there is no need to use the location information to perform the LROC analysis.

ROC curves were formed by plotting the true positive fraction against the false positive fraction for each confidence level. A ROC curve was computed for each imaging technique and for each reader. The area underneath the ROC curve was also computed for quantitatively comparing the performances of the CR and SF techniques. The results indicate that for detection of the microcalcifications, the conventional screen-film mammography technique outperforms our high resolution CR system. However, for detection of the masses, our high resolution CR system outperforms the screen-film system.

Figures 14 and 15 show two examples of the ROC curves obtained for detection of the microcalcifications. In each figure, the ROC curve for CR is plotted along with that for the SF technique for comparison. Each figure corresponds to a different reader. The areas under the ROC curves are 0.9060 for SF versus 0.7259 for CR for Reader 1 (Figure 14) and 0.8368 for SF versus 0.7366 for CR for Reader 2 (Figure 15). The results clearly shows that despite variation among readers the SF images perform better than the CR images in detecting microcalcifications.

A similar ROC study for detection of simulated masses has also been conducted. Data from a preliminary ROC study were similarly analyzed. Figures 16 shows an example of the ROC curves for the detection of masses. The areas under the ROC curves are 0.9655 for the CR technique versus 0.8270 for SF technique. The results show that for detection of masses the CR images perform significantly better than the SF images.

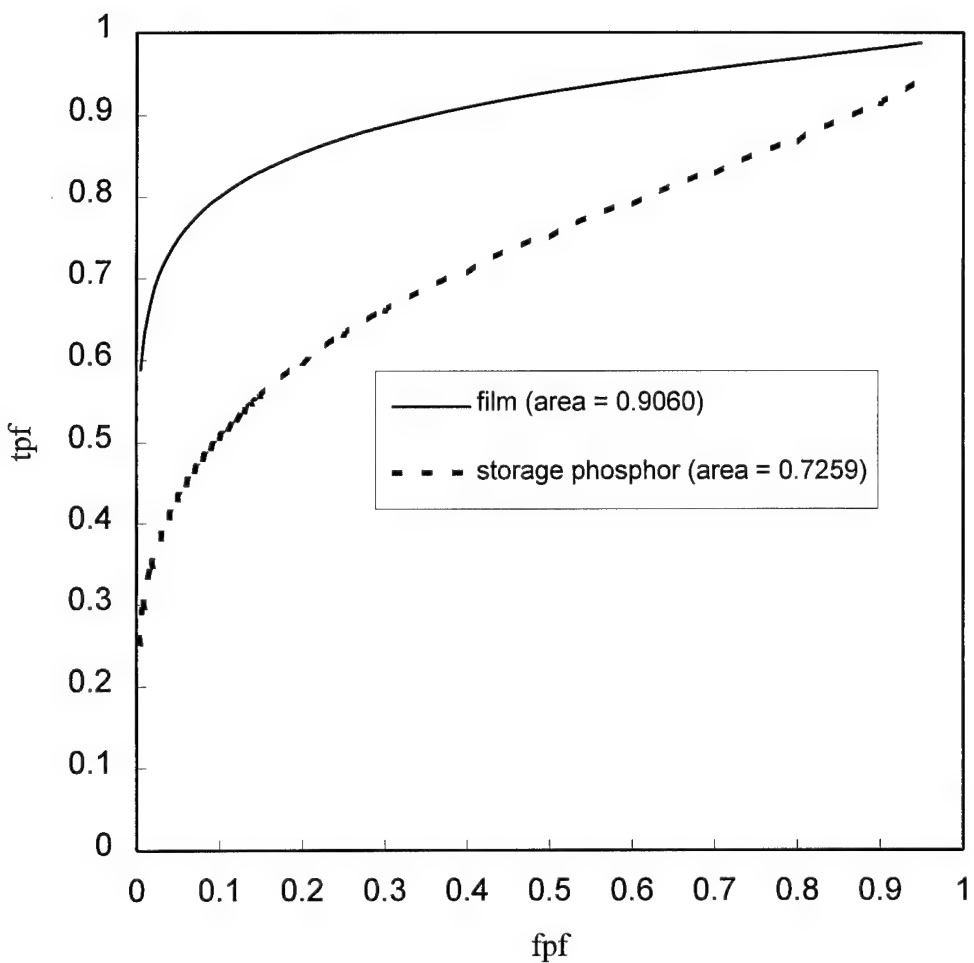


Figure 14 ROC curves for detecting the simulated microcalcifications: computed radiography versus screen-film mammography techniques (Example 1).

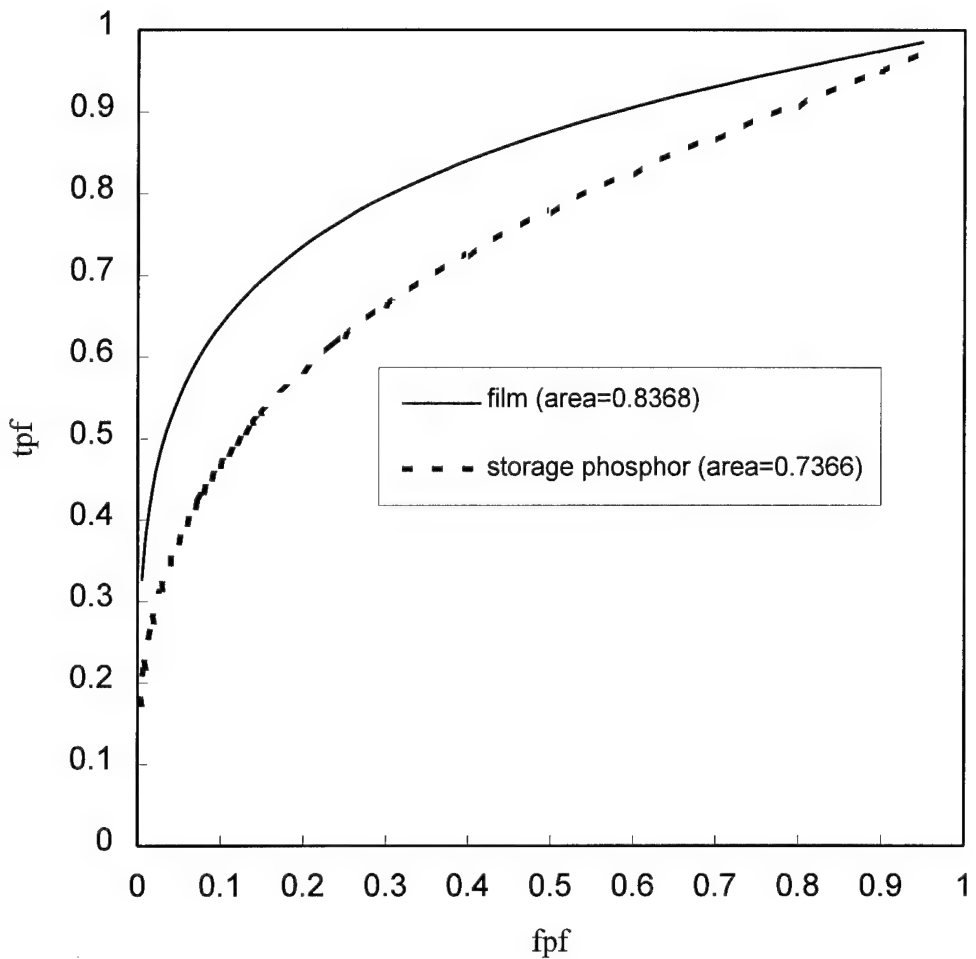


Figure 15 ROC curves for detecting the simulated microcalcifications: computed radiography versus screen-film mammography techniques (Example 2).

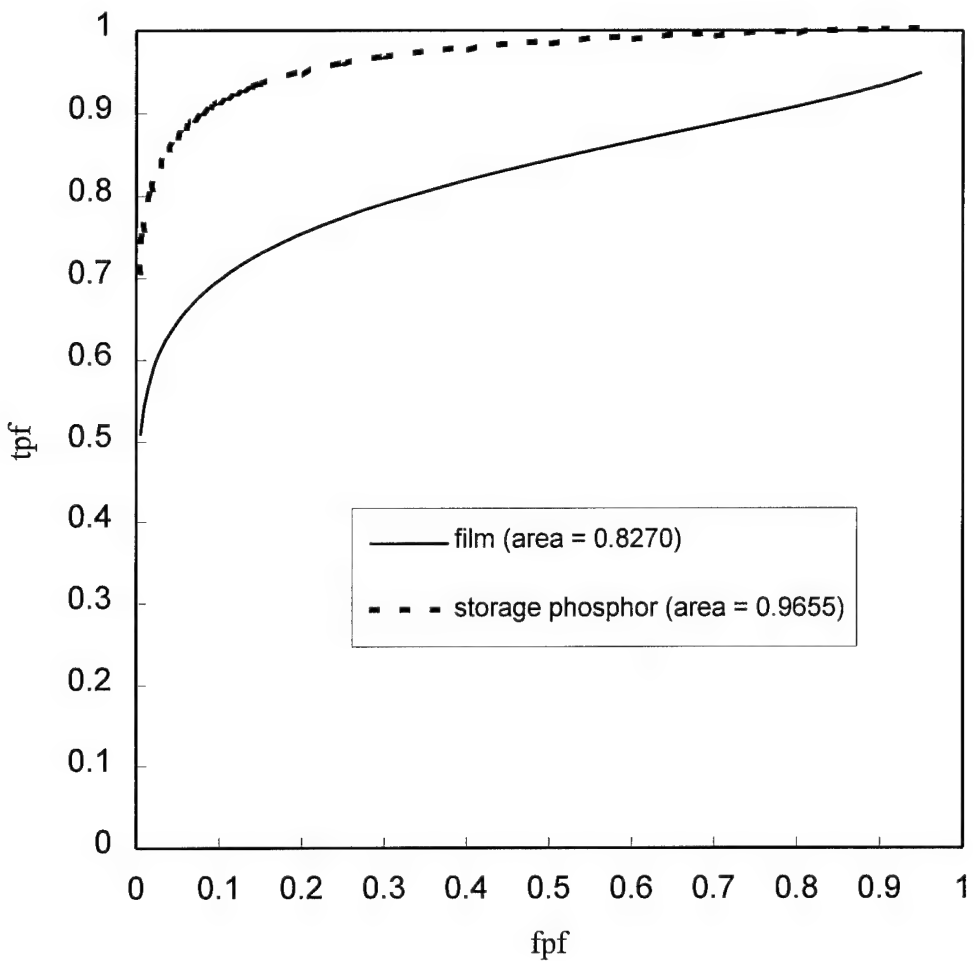


Figure 16 ROC curves for detecting the simulated microcalcifications: computed radiography versus screen-film mammography techniques (Example 1).

COMPRESSION OF IMAGE DATA

Two methods were used to develop and implement algorithms for compression of digital mammographic image data. The first method is a lossless scheme which employs image segmentation technique to eliminate data outside the breast area. The second method uses JPEG image data compression algorithm to reduce image data in a lossy fashion. Although this algorithm has been investigated for image data compression in other imaging applications⁸⁷, it must be customized for application to mammographic images. This algorithm also results in irreversible change of image data. Therefore, comparison studies were performed to determine the parameters used in the algorithm. Upon development and optimization of the algorithm, more vigorous comparison studies will be performed to validate the algorithm by ensuring that no significant loss of image quality has been incurred.

The data compression procedure developed so far can be divided into two parts: preprocessing and Joint Photographic Experts Group (JPEG) compression. They are summarized in this section. A detailed description and discussion of the methods are presented in the manuscript reprint attached as Appendix V.

Preprocessing

Before applying the JPEG compression algorithm, the image data is preprocessed to improve its compressibility. This preprocessing operation is divided into two phases; first the image is segmented and cropped and the background pixel values are modified to minimize the storage requirements for the background. We begin the segmentation process by automatically determining a threshold value from the histogram of the digitized source image that indicates the transition between background values and tissue values. This threshold value is used to classify pixels in the image as either tissue or background so as to produce a two-valued mask corresponding to the tissue-background separation.

The second phase of preprocessing involves the application of a noise-removal filter to the tissue area of the image. The particular filter tested here is a nonlinear order filter that was designed to modify mainly pixels with large noise components while leaving the majority of pixels unchanged.

JPEG Compression

The JPEG compression algorithm used in this study is a software package written and tested in our laboratory that implements the 12-bit version of the extended JPEG standard. For this study, Huffman encoding was used to encode the quantized coefficients and all compression ratios were based on this. The Huffman tables were derived from the statistics of each individual quantized image rather than on the ensemble

statistics. Signaling information was not included in the code size when calculating compression ratios.

Evaluation

The compression technique is evaluated by its speed, compression ratio and ability to preserve image information. Measurement of the compression and decompression speed is straightforward. The results, however, are dependent upon individual images. Therefore, we evaluated and compared the average speeds for the 8 images used in our study.

The purpose of preprocessing is to increase the information content in the image. Thus, we measured the average number of bits for each 8x8 pixel block of tissue area before and after segmentation. An improvement factor is computed as the ratio of average number of bits before the segmentation to that after the segmentation. We also measured the percentage of image area with breast tissue signals.

The compression ratio and ability for information preservation are not independent of each other. It is reasonable to expect better information preservation when the compression ratio is low and vice versa. We used a just noticeable difference (JND) study to quantify the information preservation as a function of the compression ratio. From eight original mammograms, which had each been compressed at five compression ratios, a set of 40 randomized pairs of images, each consisting of one laser printed non-compressed image and one compressed image were assembled. 20 readers were asked to view the pairs side by side and forced to choose the compressed image. The readers include experienced radiologists, physicists and engineers specializing in medical imaging. Following the study, the results are sorted according the compression ratio and the percentage of correctly selected pairs is plotted as a function of the compression ratio for a group of "expert readers" and a group of "average readers".

We will summarize our results from the data compression study in regard to three topics: speed of our compression system, performance of preprocessing and performance of the JPEG compression. A manuscript is attached as Appendix V for a more detailed description and discussion of the results.

Speed

The speed of our compression system is somewhat image dependent. It averages about 20 s/Mbyte to preprocess and compress source data. Decompression is faster at 15 s/Mbyte because there is no preprocessing involved. These speeds may not be acceptable for clinical use with a picture archival and communication system (PACS). However, they can be easily improved by using dedicated and optimized hardware as much as possible.

Preprocessing

A summary of the effect of image segmentation on the number of bits needed to represent tissue blocks is shown in Table 1 in which the percentage of image area containing tissue signals, bits per tissue block before and after segmentation, and the improvement factor are listed for each of the 8 original mammograms. From these results, the information content of the image has been improved by a factor of 2.7 on the average despite the fact that the background only represented 36% of the image area.

JPEG Compression

In Figure 17, the performance of image processing specialists and nonspecialists, measured by the ratio of correct identification of compressed images, is plotted as a function of the compression ratio. These results verify our expectation that the higher the compression ratio is, the more information change there is and therefore the easier one can identify the compressed images. However, the impact of data compression on diagnostic accuracy must be evaluated by a ROC study.

Table 1: The Effect of Image Segmentation on Tissue Block Representation (bits per block)

Image	% of Area Representing Tissue	Bits per Tissue Block (no preprocessing)	Bits per Tissue Block (after segmentation)	Improvement Factor
1	51.1	8.6	30.1	3.5
2	52.9	8.5	27.0	3.2
3	70.5	9.1	32.3	3.5
4	71.7	10.0	28.0	2.8
5	72.4	9.4	23.6	2.5
6	56.8	7.6	26.5	3.5
7	70.7	24.2	27.4	1.1
8	67.0	18.0	22.2	1.2

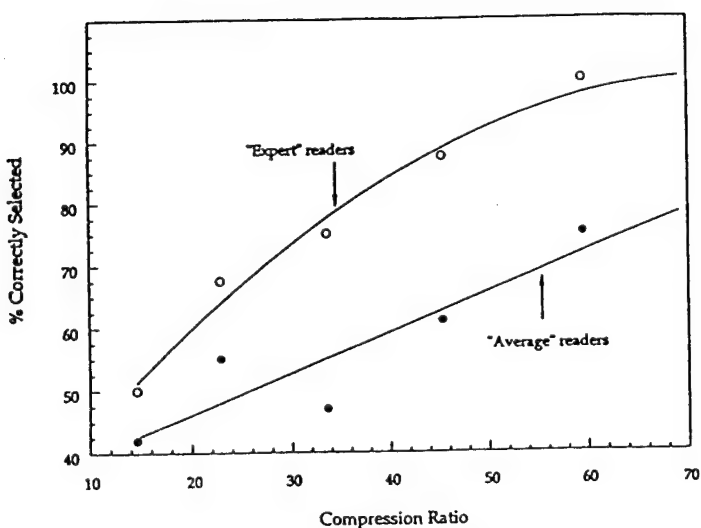


Fig 17 Performance of image-processing specialists and nonspecialists for the task of identifying compressed versus noncompressed images. 41

CONCLUSIONS

To summary our accomplishment in the grant period:

1. We have developed and implemented a technique to measure and monitor the laser beam spot size (Half Maximum Width). Furthermore, the operation was automated and sped up so that the laser beam profile and spot size can be monitored during focusing or adjustment of the beam size. With the help of this technique, we have successfully modified the optics of our storage phosphor image reader and reduced the laser beam spot size to approximately $30\mu\text{m}$ (Half Maximum Width).
2. We have measured and studied the characteristics of of our CR system. A Fourier transform technique was developed to measure the MTF of digital imaging system with images of commercial resolution bar patterns. Using this technique, the MTF's of our system were measured and compared with those of a typical commercial system. Effects of reduced laser beam spot and CR screens were also studied. A quality control protocol has been developed and used to check the performance of our CR system during the course of our project.
3. We have developed a perception phantom for evaluating and monitoring the low contrast performance of mammographic imaging systems. Using this phantom and two other phantoms, a series of images were acquired and used to study the effects of reduced laser beam spot and screen selection in CR mammography and to compare the CR with SF systems for mammographic imaging.
4. We have designed and constructed phantoms for the ROC studies. Using these phantoms, we have acquired both CR and SF images to simulate the task for detecting microcalcifications and the task for detecting masses. The CR images were printed with a pixel size of $50\mu\text{m}$ for the reading studies. Software for acquiring and analyzing the reading studies were developed. Reading experiments have been conducted. ROC curves have been obtained to compare the CR with the SF techniques.
5. We have developed a JPEG based algorithm for compressing mammographic image data. A Just Noticeable Difference (JND) study was conducted to quantify the information preservation as a function of the compression ratio.

The above studies have resulted the following conclusions:

1. We have demonstrated it is feasible to configure a CR system for high resolution imaging applications like mammography. It is possible to modify the laser scanning optics to reduce the laser beam spot size down to $40\mu\text{m}$ or even smaller.

2. The reduction of the laser beam spot size and use of a high resolution CR screen result in a significant improvement of the spatial resolution capability of the storage phosphor imaging system. This improvement allows us to visually resolve 10 lps/mm bar patterns at 25 kVp on a mammographic unit. The MTF's of the improved CR system significantly exceed those of a typical commercial system. The greater detection efficiency from using a thicker screen (ST screen) is more than offset by the loss of MTF.
3. Commercial phantoms alone can not differentiate the subtle performance differences between the CR and SF techniques. The use of aluminum wires with finely spaced sizes help differentiate the performance difference between the CR and SF techniques. Comparison with phantom images show that the performance of our CR system approach but is slightly lower than that of a conventional SF mammography system. However, from the perspective of visual appearance, the difference is rather subtle.
4. Our ROC studies indicate that for the detection of microcalcifications, the SF images perform better than the CR images. For detection of masses, the CR images seem to perform better than the SF images.
5. The results of our data compression studies indicate that the detectable information change increases with compression ratio. However, the visual detection of information change may not be directly related to diagnosis. Direct impact of data compression on diagnostic accuracy must be evaluated by a ROC study which is beyond the scope of our image compression study.

The implications of these conclusions are as follows:

While our CR system has been significantly improved by reducing the laser beam spot size, it could benefit from further improvement of spatial resolution for the task of detecting small microcalcifications (less than 150 μ m in dimension). However, detection of such small microcalcifications is rather infrequent in conventional mammography. Therefore, its role in screening breast cancer is questionable. If detection of microcalcifications with a dimension of smaller than 150 μ m is essential to diagnosis, then further improvement of the spatial resolution quality of CR imaging is called for. As the laser beam spot size has been greatly reduced to an extent that the MTF degradation is rather insignificant, further increase of the MTF should be achieved by improving the design of CR image plates used for exposure rather than further reduction of the laser beam spot size. This requires the development of either a more efficient screen material to reduce the screen thickness or a structured CR screen to eliminate or reduce lateral diffusion of the laser beam.

REFERENCES*

1. Fuhrman CR, Gur D, Good BC, et al. The diagnostic quality of storage phosphor radiographs compared to conventional films: interpreter's perception. *AJR* 1988; 150:1011-14.
2. Fuhrman CR, Gur D, Schaetzing R. High resolution digital imaging with storage phosphors. *J Thoracic imaging* 1990; 5:12-30.
3. Gur D, Deutsch M, Fuhrman CR, et al. The use of storage phosphors for portal imaging in radiation therapy: therapists's perception of image quality. *Med Phys* 1989; 16(1):132-6.
4. Weiser JC, Gur D, Cano E, Deutsch M, Wu A, Mogus R. Verification of electron beam therapy with storage phosphor images: precision of field placement. *Radiol* 1990; 175:257-259.
5. Slasky BS, Gur D, Good WF, Costa-Greco MA, Harris KM, Cooperstein LA, Rockette HE. Receiver operating characteristic analysis of chest image interpretation with conventional, laser-printed, and high-resolution workstation images. *Radiol* 1990; 174:775-780.
6. Rosenthal MS, Good WF, Costa-Greco MA, Miketic LM, Eelkema EA, Gur D, Rockette HE. The effect of image processing on chest radiograph interpretations in a PACS implementations in a PACS environment. *Invest Radiol* 1990; 25:897-901.
7. Schaetzing R, Whiting BR, Lubinsky AR, Owen JF. Digital radiography using storage phosphors. in *Digital imaging in diagnostic radiology*, published by Churchill Livingstone (1989).
8. Hillen W, Schievel U, Zaengel T. Imaging performance of a digital storage phosphor system. *Med Phys* 1987;14:744.
9. Fujita H, Ueda K, Morishita J, Fujikawa T, Ohtsuka A, Sai T. Basic imaging properties of a computed radiographic system with photostimulable phosphors. *Med Phys* 1989;16(1):338-345.
10. Lubinsky AR, Owen JF, Korn DM. Storage phosphor system for computed radiography: screen optics. *SPIE* 1986;626:120-132.
11. Lubinsky AR, Whiting BR, Owen JF. Storage phosphor system for computed radiography: optical effects and detective quantum efficiency (DQE). *SPIE* 1987;767:167-177.
12. Fujita H, Ueda K, Ohtsuka A. Resolution property of digital radiography with photostimulable phosphors. I. Measurements of imaging plate MTF's. *Jpn J Med Imag Inform Sooc* 1987; 4:89.
13. Fujita H, Ueda K, Fujikawa, Ohtsuka A. Resolution property of digital radiography with photostimulable phosphors. II. Measurements of digital characteristic curve and presampling MTF. *Jpn J Med Imag Inform Sooc* 1988; 5:1.
14. Shaw CC, Herron JM, Gur D. Signal fading, erasure and rescan in storage phosphor imaging. *SPIE* 1992;1651 *Image Physics*. In press.
15. Bunch PC. Detective quantum efficiency of selected mammographic screen-film combinations. *Proc SPIE* 1989; 1090:67-77.

16. Silverberg E, Lubera JA: A Review of American Cancer Society estimates of cancer cases and deaths. CA 1983; 33:2-8.
17. Silverberg E: Cancer statistics, 1983. Ca 1983; 33:9-25.
18. Nathan S: An Atlas of Normal and Abnormal Mammograms. Oxford; New York; Oxford University Press, 1982.
19. Feig SA, McLelland R, Eds: Breast Carcinoma: Current Diagnosis and Treatment. New York, Masson Publishing USA, Inc, and the American College of Radiology, Chicago, 1983.
20. National Task Force on Breast Cancer Control: Mammography: A statement of the American Cancer Society. Conn Med 1983; 47:37-9.
21. Moskowitz M, Gartside PS: Evidence of breast cancer mortality reduction: Aggressive screening in women under age 50. AJR 1982; 138:911-6.
22. Venet L, Shapiro S, Strax P, Venet W: Effect of screening on survivals. In: Early Breast Cancer/Detection and Treatment, New York, John Wiley & Sons, 1975.
23. Pavlov KA, Semiglazov VF: Detection of early forms of breast cancer by mass screening examinations. Neoplasma 1981; 28:611-5.
24. Breast Cancer Digest 1979; 80:1691.
25. Strax P: Control of breast cancer through mass screening. JAMA 1976; 235:1600-2.
26. Thomas BA, Price JL, Boulter PS. Breast cancer population screening by single view mammography with selective clinical examination--A pilot study. Clin Oncol 1981; 7:201-4.
27. Tabar L, Gad A: Screening for breast cancer: The Swedish trial. Radiology 1981; 138:219-22.
28. Andersson I, Andren L, Hildell J, Linell F, Ljungqvist U, Pettersson H: Breast cancer screening with mammography. Radiology 1979;273-6.
29. Beahrs OH, Shapiro S, Smart C: Report of the working group to review the NCI/ACS breast cancer detection demonstration projects. NCI 1977.
30. Beahrs OH, Shapiro S, Smart CH, et al: Report of working group to review BCDDP. J Natl Cancer Inst 1979; 62:679-90.
31. Strax P: Organization of mass screening programs in breast cancer--Including identification of high-risk groups. In: Early Diagnosis of Breast Cancer, Grundman E, Beck L, Eds. Stuttgart, Gustav Fischer Verlag, 1978.
32. Lundgren B, Helleberg A: Single oblique-view mammography for periodic screening for breast cancer in women. JNCI 1982; 68:351-5.
33. Haus AG: Physical principles and radiation dose in mammography. Med Radiogr Photogr 1982; 58:70-80.
34. Moskowitz M, Gartside PS, Gardella L, deGroot I, Guenther D: The breast cancer screening controversy: A perspective. In: Breast Carcinoma: The Radiologist's Expanded Role. Logan WW, Ed. New York, John Wiley & Sons, 1977, pp 35-52.
35. Moskowitz M: Screening for breast cancer: How effective are our tests? A critical review. CA 1983; 33:26-39.
36. Moskowitz M: Mammographic screening: Significance of minimal breast cancers. AJR 1981; 136:735-8.

37. Leborgne RA: The Breast in Roentgen Diagnosis. London, Constable and Co., 1953.
38. Ingleby H, Gershon-Cohen J: Comparative Anatomy, Pathology and Roentgenology of the Breast. Philadelphia, University of Pennsylvania Press, 1960.
39. Stanton L, Villafana T, Day JL, Lightfoot DA: A breast phantom method for evaluating mammography technique. Invest Radiol 1978; 13:291-7.
40. Miller DW: Center for Radiological Physics: Mammography Review Procedures and Results. In: Breast Carcinoma: The Radiologist's Expanded Role. Logan WW, Ed. New York, John Wiley & Sons, 1977, pp 129-33.
41. Porrath SA: XERG mammography: A review of sixteen months experience plus a comparison with xeromammography. In: Logan W, Muntz EP, Reduced Dose Mammography. New York, Masson Publishing USA, 1979, pp 389-94.
42. Hirschfeld RL: XERG and lo-dose mammography: A comparative clinical study. In: Logan WW, Muntz EP: Reduced Dose Mammography. New York, Masson Publishing USA, 1979, pp 395-405.
43. Sickles EA: Heavy-particle mammography. In: Breast Carcinoma: The Radiologist's Expanded Role. Logan WW, Ed. New York, John Wiley & Sons, 1977, pp 239-41.
44. Isard HJ: General discussion: Thermography in the mass screening of cancer. Ann NY Acad Sci 1980; 335:520-3.
45. Milbrath JR: Does thermography aid in breast cancer detection? In: Breast Carcinoma: The Radiologist's Expanded Role. Logan WW, Ed. New York, John Wiley & Sons, 1977, pp 255-8.
46. Chang CHJ, Sibala JL, Fritz SL, Dwyer SJ III, Templeton AW: Specific value of computed tomographic breast scanner (CT/M) in diagnosis of breast diseases. Radiology 1979; 132:647-52.
47. Gisvold JJ, Karsell PR, Reese DF: Computerized tomographic mammography. In: Breast Carcinoma: The Radiologist's Expanded Role. Logan WW, Ed. New York, John Wiley & Sons, 1977, pp 219-38.
48. Bryan RN, Hazelwood CF, Ford JJ, Fisher PB, Schneiders NJ, Garnil E: In vivo NMR imaging of the human breast. Presented at the 69th Annual Meeting of the Radiological Society of North America, Chicago, 1983.
49. Sickles EA, Davis PL, Crooks LE: NMR characteristics of benign and malignant breast tissues: Preliminary report. Presented at the 69th Annual Meeting of the Radiological Society of North America, Chicago, November 1983.
50. El-Yousef SJ, O'Connell DM, Duchesneau RH, et al. Radiofrequency pulse sequences for characterization of benign and malignant conditions of the breast. Radiology 1984; 153:52.
51. Cole-Beuglet C, Baltarowich O, Pasto ME, Rifkin MD, Kurtz AB, Goldberg BB: Ultrasound appearance of carcinoma in younger patients. Presented at the 69th Annual Meeting of the Radiological Society of North America, Chicago, November 1983.

52. McSweeney MB, Egan RL: Solid breast masses: Ultrasonographic, mammographic, and pathologic correlation. Presented at the 69th Annual Meeting of the Radiological Society of North America, Chicago, November 1983.
53. Muntz EP, Wilkinson E, George FW: Mammography at reduced doses: Present performance and future possibilities. AJR 1980; 134:741-7.
54. Jennings RJ, Eastgate RJ, Siedband MP, Ergun DL: Optimal x-ray spectra for screen-film mammography. Med Phys 1981; 8:629-39.
55. Brodie I, Gutcheck RA: Radiographic information theory: Correction for x-ray spectral distribution. Med Phys 1983; 10:293-300.
56. Barnes GT, Chakraborty DP: Radiographic mottle and patient exposure in mammography. Radiology 1982; 145:815-21.
57. Egan RL, McSweeney MB, Sprawls P: Grids in mammography. Radiology 1983; 146:359-62.
58. Barnes GT: Radiographic mottle: A comprehensive theory. Med Phys 1982; 9:956-67.
59. Zarand P, Pentek: Absorbed dose in "high filtration" xeromammography--An intercom parison. Radiol Diagn 1981; 22:240-6.
60. Sickles EA: Mammographic detectability of breast micro- calcifications. AJR 1982; 139:913-8.
61. Haus AG: Effect of geometric unsharpness in mammography and breast xeroradiography. In:Breast Carcinoma: The Radiologist's Expanded Role. Logan WW, Ed. New York, John Wiley & Sons, 1977, pp 93-108.
62. Brodie I, Gutcheck RA: Radiographic information theory and application to mammography. Med Phys 1982; 9:79-95.
63. Dodd GD: Radiation detection and diagnosis of breast cancer. Cancer 1981; 47:1766-9.
64. Hammerstein GR, Miller DW, White DR, Masterson ME, Woodard HQ, Laughlin JS: Absorbed radiation dose in mammography. Radiology 1979; 130:485-91.
65. Haus AG. Technologic improvements in screen-film mammography. Radiology 1990; 1174:628-37.
66. Haus AG. Recent trends in screen-film mammography: technical factors and radiation dose. Recent Results Cancer Res 1987; 105:37-51.
67. Haus AG. Recent advances in screen-film mammography. Radiol Clin north Am 1987; 25:913-28.
68. Sickles EA: Mammographic detectability of breast microcalcifications. AJR 1982; 139:913-8.
69. Muir BB, Lamb J, Anderson TJ, Kirkpatrick AE: Microcalcification and its relationship to cancer of the breast: Experience in a screening clinic. Clin Radiol 1983; 34:193-200.
70. Chan HP, Vyborny CJ, MacMahon H, Metz CE, Doi K, Sickles EA. Digital mammography: ROC studies of the effects of pixel size and unsharp-mask filtering on the detection of subtle microcalcifications. Invest Radiol 1987; 22:581-9.
71. Chan HP, Doi K, Galhotra S, Vyborny CJ, MacMahon H, Jokich PM. Image feature analysis and computer-aided diagnosis in digital radiography. I. Automated detection of microcalcifications in mammography. Med Phys 1987; 14:538-48.

72. Belikova TP, Yaroslavsky LP. Comments on "Image feature analysis and computer-aided diagnosis in digital radiography. I. Automated detection of microcalcifications in mammography." letter to Med Phys 1989; 16:142.
73. Chan HP, Doi K, Vyborny CJ, Schmidt RA, Metz CE, Lam KL, Ogura T, Wu YZ, MacMahon H. Improvement in radiologists' detection of clustered microcalcifications on mammograms: the potential of computer-aided diagnosis. Invest Radiol 1990; 25:1102-10.
74. Fam BW, Olson SL, Winter PF, Scholz FJ. Algorithm for the detection of fine clusttered calcifications on film mammograms. Radiology 1988; 169:333-7.
75. Dhawan AP, Le Royer E. Mammographic feature enhancement by computerized image processing. Comput Methods Programs Biomed 1988; 27:23-35.
76. Davies DH, Dance DR. Automatic computer detection of clustered calcifications in digital mammograms. Phys Med Biol 1990; 35:1111-8.
77. Fujita H, Ueda K, Ohtsuka A. Resolution property of digital radiography with photostimulable phosphors. I. Measurements of imaging plate MTF's. Jpn J Med Imag Inform Sooc 1987; 4:89.
78. Fujita H, Ueda K, Fujikawa, Ohtsuka A. Resolution property of digital radiography with photostimulable phosphors. II. Measurements of digital characteristic curve and presampling MTF. Jpn J Med Imag Inform Sooc 1988; 5:1.
79. Barnes GT, Sones RA, Tesic MM. Digital chest radiography: performance evaluation of a prototype unit. Radiology 1985; 154:801-806
80. Doi K, Fujita H, Ohara K, et al. Digital radiographic imaging system with multiple slit scanning x-ray beam: preliminary report. Radiology 1986; 161:513-518.
81. Templeton AW, Dwyer III SJ, Cox GG, et al. A digital radiology imaging system: description and clinical evaluation. AJR 1987; 149:847-851.
82. Slasky BS, Sashin D, et al. Digital radiography of the chest by self-scanning linear diode arrays. Acta Radop;pgica 1987; 28:461-466.
83. Fritz SL, Chang CH, Gupta NK, Martin NL, Laws RL, Anderson WH, Dwyer SJ, Templeton AW, Bernardi R, Fox T. A digital radiographic imaging system for mammography. Invest Radiol 1986; 21:581-3.
84. Rosenthal MS, Sashin D, Herron J, Maitz G, Boyer J, Gur D. Evaluation of a moving slit technique for mammography. SPIE 1991;1443 Medical Imaging V- Image Physics:132-142.
85. Nishikawa RM, Mawdsley GE, Fenster A, Yaffe MJ. Scanned-projection digital mammography. Med Phys 1987; 14:717-27.
86. Holdsworth DW, Gerson RK, Fenster A. A time-delay integration charge-coupled device camera for slot-scanned digital radiography. Med Phys 1990; 17:876-86.
87. Good WF. Bit allocation tables for the compression of chest images by JPEG type algorithms. SPIE 1992;1652 Image Processing. In press.
88. Photometrics. Charge-coupled devices for quantitative electronic imaging. 1991. Tuscon: Photometrics Ltd. 1-28.
89. Kennedy WH, Herron JM, Gur D, et al. X-ray imaging with two-dimensional CCD arrays. Med Phys 1985; 12(4):504.

90. Herron JM, Gur D, Daxon EG, Good WF, Shaw CC, et al. Digital x-ray imaging with two-dimensional charge-coupled device (CCD) arrays. Proc SPIE 1990; 1231:472-478.
91. Lawrence JL, Cope AD, Herron JM, et al. Medical x-ray imaging applications of the TEK2048 CCD. Proc SPIE 1990; 1242:59-65.
92. Kimme-Smith C, Bassett LW, Gold RH, Gormley L. Digital mammography: a comparison of two digitization methods. Invest Radiol 1989; 24:869-75.
93. Oestmann JW, Kopans D, Hall DA, McCarthy KA, Rubens JR, Greene R. A comparison of digitized storage phosphors and conventional mammography in the detection of malignant microcalcifications. Invest Radiol 1988; 23:725-8.
94. Kato Hisatoyo. Photostimulable phosphor radiography: design considerations. Proc AAPM Summer School: Specification, Acceptance Testing and Quality Control of Diagnostic X-ray Imaging Equipment 1991.
95. Melles Griot Optics guide. Vol. 5, Chapters 17-21, 1991.
96. Stanton L, Day JL, Villafana T, Miller CH, Lightfoot DA. Screen-film mammographic technique for breast cancer screening. Radiology 1987; 163:4771-9.
97. Goodman LR, et al. Digital and conventional chest images:observer performance with film digital radiography system. Radiology 1986; 158:27-33.
98. Hanley JA, McNeil BJ. The meaning and the use of the area under a receiver operating characteristic (ROC) curve. Radiol 1982; 143:29-36.
99. Hanley JA, McNeil BJ. A method of comparing the areas under receiver operating characteristic curves derived from the same cases. Radiol 1983; 148:839-843.
100. Kelsey CA, Mettler FA. ROC analysis can reveal best diagnostic method. Diagnost Imag 1989; 155-161.
101. McNeil BJ, Hanley JA. Statistical approaches to the analysis of receiver operating characteristic (ROC) curves. Med Decis Making 1984; 4:137-150.
102. Metz CE. ROC methodology in radiologic imaging. Invest Radiol 1986; 21:720-733.
103. Swets JA. ROC analysis applied to the evaluation of medical imaging techniques. Invest Radiol 1979; 14:109-121.
104. Swets JA, Pickett RM. Evaluation of diagnostic systems: methods from signal detection theory. New York: Academic Press 1982.
105. Rockette HE, Gur D, Cooperstein LA, Obuchowski NA, King JL, Fuhrman CR, Tabor EK, Metz CE. Effect of two rating formats in multi-disease ROC study of chest images. Invest Radiol 1990;25:225-29.
106. Gur D, Rockette HE, Good WF, Slasky BS, Cooperstein LA, Straub WH, Obuchowski NA, Metz CE. Effect of observer instruction on ROC study of chest images. Invest Radiol 1990;25:230-34.
107. Rockette HE, Obuchowski NA, Gur D. Non-parametric estimation of degenerate ROC data sets used for comparison of imaging systems. Invest Radiol 1990;25:835-37.
108. Rockette HE, Gur D, Metz CE. The use of continuous and discrete confidence judgments in Receiver Operating Characteristic studies of diagnostic imaging techniques. Invest Radiol 1992;27:169-172.

109. Caldwell CB, Yaffe MJ, "Development of an anthropomorphic breast phantom", Med Phys 1990; 17(2): .
110. Screen film mammography: Imaging considerations and medical physics responsibilities, Ed. by Gary Barnes and G. Donald Frey, Medical Physics Press, Madison, WI, 1991.
111. AAPM Report No. 29: Equipment requirement and quality control for mammography, Ed. by M. J. Yaffe et al, Published for the American Association of Physicists in Medicine by the American Institute of Physics.
112. Good WF, Maitz GS, Gur D. Joint photographic experts group (JPEG) compatible data compression of mammograms. J Digi Imag, 1994; 7(3): 123-132.
113. Shaw CC, Herron JM, Wang T, Breitenstein D. High-resolution storage phosphor imaging with reduced laser beam spot size in image readout. Abstract in Radiology, 1994; 193(P): 251.

** For convenience, this reference list was adopted from the original proposal. However, the list has been updated and several new references were added. It should be noted that not all references are cited in this report.*

APPENDIX I

SPECIFICATIONS FOR THE RESOLUTION TEST PATTERN (Nuclear Associates, Model 07-553)

Figure 1 is an enlarged contact radiograph of the test plate. The spacing of the bar pattern varies in steps between the index marks. For example, the spatial frequency of the pattern between AB is one-half line pair per millimeter and the spatial frequency between CD is 0.85 line pairs per millimeter.

Table #1 tabulates the spatial frequency associated with each of the index marks. A larger line separates the pattern into a group of line pairs with longer lines corresponding to groups of 0.5, 1, 2, 5 and 10 line pairs per millimeter.

Fig. 1

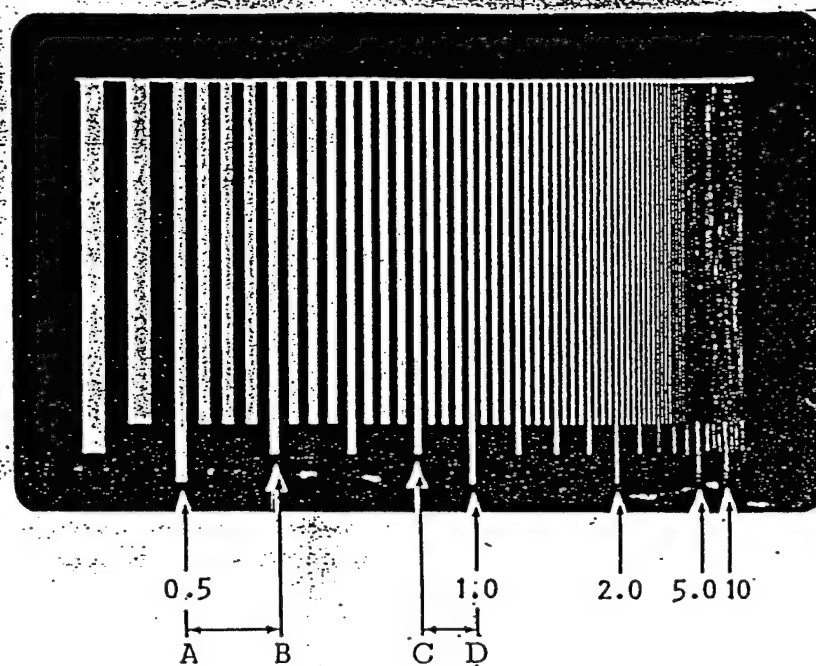


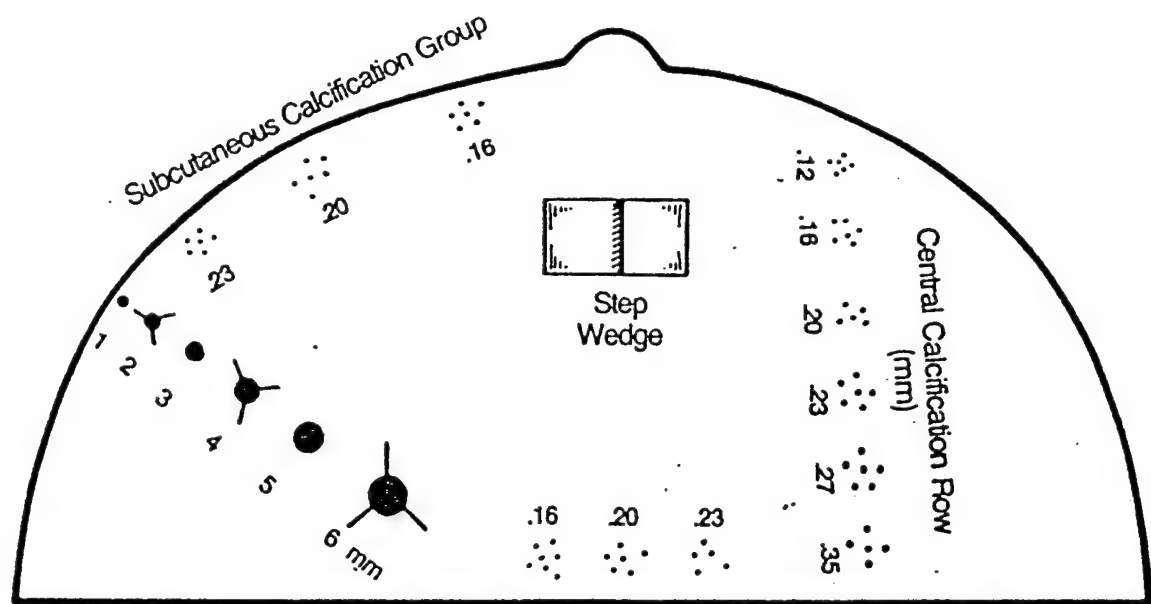
Table #1 The line pairs/mm value for each resolution group is listed below.

Group	LP/mm					
1	0.25	7	1.2	13	3.5	19 <u>10</u>
2	<u>0.5</u>	8	1.4	14	4.2	20 8.5
3	0.6	9	1.7	15	<u>5.0</u>	21 7
4	0.7	10	<u>2.0</u>	16	6	22 6
5	0.85	11	2.4	17	7	
6	<u>1.0</u>	12	2.9	18	8.5	

APPENDIX II

SPECIFICATIONS FOR THE CIRS BREAST PHANTOM (Computerized Imaging Reference Systems, Inc.)

Map of Embedded Details in Phantoms.



- **Stepwedge**
5 mm glandular equivalent/5 mm fat equivalent
- **Microcalcifications (CaCO_3)**
12 groupings with largest at .35 mm diameter and smallest at .12 mm diameter. This range of sizes has been shown in practice to be sensitive to system calibration and performance.

- **Masses**
6 simulated tumor masses ranging from 6 mm diameter to 1 mm diameter
- **Fibrils**
3 fibre spiculations

CIRS COMPUTERIZED IMAGING
REFERENCE SYSTEMS, INC.

2488 Almeda Avenue, Norfolk, Virginia 23513
Tel: (804) 855-2765

APPENDIX III

SPECIFICATIONS FOR THE ANTHROPOMORPHIC BREAST PHANTOM (Model 165, Gammex-Radiation Measurement Inc.)

Specifications

Breast Tissue Equivalent Plastic Casting	Tissue Equivalent Plastic, RMI Model 454 50% adipose, 50% glandular, (BR-12 equivalent)
High Resolution Layer	Radiographic film containing a stable mercury-silver amalgam.
	9 step gray level stepwedge.
	Resolution Bar Pattern: 5-25 lp/mm
Phantom Case	Case Material: Acrylic Top Thickness: 0.215 in Bottom Thickness: 0.175 in
Overall Dimensions	19.6 x 11.7 x 6.1 cm (7.7 x 4.7 x 2.4 in)
	0.7 kg (1.6 lb)

Note: Due to our philosophy of continuous product improvement, these specifications may change without notice.

APPENDIX IV

Captions for Attached Films

- Film 1 Image of a resolution bar pattern obtained with a screen-film mammography system. Exposures were made at 25kVp, 6mAs and a source-to-image distance of 65cm.
- Film 2 CR image of a resolution bar pattern obtained with a ST screen, a laser beam diameter of 30 μ m and a pixel size of 43 μ m were used. Exposures were made at 25kVp, 10mAs and a source-to-image distance of 65cm.
- Film 3 CR image of a resolution bar pattern obtained with a HR screen, a laser beam diameter of 30 μ m and a pixel size of 43 μ m were used. Exposures were made at 25kVp, 10mAs and a source-to-image distance of 65cm.
- Film 4 CR image of a resolution bar pattern obtained with a HR screen, a laser beam diameter of 50 μ m and a pixel size of 43 μ m were used. Exposures were made at 25kVp, 10mAs and a source-to-image distance of 65cm.
- Film 5 Image of a perception phantom obtained with a screen-film mammography system. Exposures were made at 25kVp, 22mAs and a source-to-image distance of 65cm.
- Film 6 CR image of a perception phantom obtained with a ST screen, a laser beam diameter of 30 μ m and a pixel size of 43 μ m were used. Exposures were made at 25kVp, 22mAs and a source-to-image distance of 65cm.
- Film 7 CR image of a perception phantom obtained with a HR screen, a laser beam diameter of 30 μ m and a pixel size of 43 μ m were used. Exposures were made at 25kVp, 22mAs and a source-to-image distance of 65cm.
- Film 8 CR image of a perception phantom obtained with a HR screen, a laser beam diameter of 50 μ m and a pixel size of 43 μ m were used. Exposures were made at 25kVp, 22mAs and a source-to-image distance of 65cm.
- Film 9 Image of a tissue equivalent breast phantom obtained with a screen-film mammography system. Exposures were made at 25kVp, 144mAs and a source-to-image distance of 65cm.
- Film 10 CR image of a tissue equivalent breast phantom obtained with a ST screen, a laser beam diameter of 30 μ m and a pixel size of 43 μ m were used. Exposures were made at 25kVp, 144mAs and a source-to-image distance of 65cm.

- Film 11 CR image of a tissue equivalent breast phantom obtained with a HR screen, a laser beam diameter of 30 μm and a pixel size of 43 μm were used. Exposures were made at 25kVp, 144mAs and a source-to-image distance of 65cm.
- Film 12 CR image of a tissue equivalent breast phantom obtained with a HR screen, a laser beam diameter of 50 μm and a pixel size of 43 μm were used. Exposures were made at 25kVp, 144mAs and a source-to-image distance of 65cm.
- Film 13 Image of an anthropomorphic breast phantom obtained with a screen-film mammography system. Exposures were made at 25kVp, 104mAs and a source-to-image distance of 65cm.
- Film 14 CR image of an anthropomorphic breast phantom obtained with a ST screen, a laser beam diameter of 30 μm and a pixel size of 43 μm were used. Exposures were made at 25kVp, 104mAs and a source-to-image distance of 65cm.
- Film 15 CR image of an anthropomorphic breast phantom obtained with a HR screen, a laser beam diameter of 30 μm and a pixel size of 43 μm were used. Exposures were made at 25kVp, 104mAs and a source-to-image distance of 65cm.
- Film 16 CR image of an anthropomorphic breast phantom obtained with a HR screen, a laser beam diameter of 50 μm and a pixel size of 43 μm were used. Exposures were made at 25kVp, 104mAs and a source-to-image distance of 65cm.
- Film 17 CR image of a meat phantom with simulated microcalcifications. Exposures were made at 25kVp, 22mAs and a source-to-image distance of 65cm. 5mil microcalcifications are present in box #1, 2, 5, 7 and 6mil microcalcifications were simulated in box #8, 11. The boxes are numbered as shown in Figure 13.
- Film 18 SF image of a meat phantom with simulated microcalcifications. Exposures were made at 25kVp, 22mAs and a source-to-image distance of 65cm. 5mil microcalcifications are present in box #1, 2, 5, 7 and 6mil microcalcifications were simulated in box #8, 11. The boxes are numbered as shown in Figure 13.
- Film 19 CR image of a meat phantom with simulated masses. Exposures were made at 25kVp, 22mAs and a source-to-image distance of 65cm. Masses were simulated in Box #7, 9, 10, 12. The boxes are numbered as shown in Figure 13.
- Film 20 SF image of a meat phantom with simulated masses. Exposures were made at 25kVp, 22mAs and a source-to-image distance of 65cm. Masses were simulated in Box #7, 9, 10, 12. The boxes are numbered as shown in Figure 13.

APPENDIX V

**"Joint Photographic Experts Group (JPEG) Compatible Data
Compression of Mammograms"**

by Walter F. Good, Glenn S. Maitz, David Gur

**Department of Radiology, University of Pittsburgh
Pittsburgh, Pennsylvania 15261**

Published in Journal of Digital Imaging, Vol 7, No 3, 1994: pp 123-132

Joint Photographic Experts Group (JPEG) Compatible Data Compression of Mammograms

Walter F. Good, Glenn S. Maitz, and David Gur

We have developed a Joint Photographic Experts Group (JPEG) compatible image compression scheme tailored to the compression of digitized mammographic images. This includes a preprocessing step that segments the tissue area from the background, replaces the background pixels with a constant value, and applies a noise-removal filter to the tissue area. The process was tested by performing a just-noticeable difference (JND) study to determine the relationship between compression ratio and a reader's ability to discriminate between compressed and noncompressed versions of digitized mammograms. We found that at compression ratios of 15:1 and below, image-processing experts are unable to detect a difference, whereas at ratios of 60:1 and above they can identify the compressed image nearly 100% of the time. The performance of less specialized viewers was significantly lower because these viewers seemed to have difficulty in differentiating between artifact and real information at the lower and middle compression ratios. This preliminary study suggests that digitized mammograms are very amenable to compression by techniques compatible with the JPEG standard. However, this study was not designed to address the efficacy of image compression process for mammography, but is a necessary first step in optimizing the compression in anticipation of more elaborate reader performance (ROC) studies.

Copyright © 1994 by W.B. Saunders Company

KEY WORDS: Data compression, mammography, Joint Photographic Experts Group (JPEG), image processing, picture archiving and communication system.

IN RECENT YEARS, there has been a rapid increase in the use of mammography and a corresponding increase in the complexity of managing mammographic studies. Many believe that to accommodate the large number of mammographic studies now being performed, these images must be managed in a digital format. The main difficulty with this relates to the large volume of digital data needed to represent each image. High-resolution digital mammograms are likely to contain 10 to 40 Mbyte each. Digital archiving and data-transmission systems quickly become strained when called upon to deal with a large number of these images. The application of image-compression techniques has the potential to greatly reduce this problem.

Because the problems of dealing with digital image data are universal, the Joint Photographic Experts Group (JPEG) has recently

defined a general-purpose image-compression standard.¹⁻³ Because the JPEG standard does not specifically address mammographic images, our aim in this study was to develop a compression technique for digitized mammograms which is compatible with the standard, but which is optimized for mammographic images, and then to determine the level of compression that can be achieved before the effects of compression become detectable by observers.

The JPEG algorithm is a block quantization version of the cosine transform in which images are divided into 8- × 8-pixel blocks and the cosine transforms applied to each block individually. The frequency coefficients calculated from the cosine transform are quantized by dividing by values from an array of quantization factors and rounding the quotients to integral values. The resulting array of quotients is aligned in a zigzag order and then encoded by either Huffman coding or by adaptive arithmetic coding. In this method, the quantization factors that are applied to the frequency coefficients determine the compression ratio as well as the kind of information lost or artifact introduced.

The main challenge in applying JPEG standard compression relates to the need to tailor the technique to the characteristics of the particular kind of images being compressed. There are two main areas where there is flexibility in applying the standard—in the quantization of the frequency coefficients and in preprocessing the image before the application of the JPEG algorithm.

In the past, most attention has focused on the

From the Department of Radiology, University of Pittsburgh, Pittsburgh, PA.

Supported in part by Grant No. DAMD 17-93-J3009 from the Department of the Army. The content of the information included in this manuscript does not reflect the position or the policy of the government and no official endorsement should be inferred.

Address reprint requests to Walter F. Good, PhD, A439 Scaife Hall, Department of Radiology, University of Pittsburgh, Pittsburgh, PA 15261-0001.

Copyright © 1994 by W.B. Saunders Company
0897-1889/94/0703-0007\$3.00/0

design of the quantization table required in the quantization stage of the compression process. The default quantization factors, which are provided in the standard, are not adequate for most purposes—hence, the standard encourages user-specified quantization tables. But the resulting image quality is determined by the quantization table used, so the design of these tables must be optimized for the particular compression task.

The current trend is to base quantization tables on psychophysical consideration.^{4,6} This approach is somewhat controversial when the compression is to be used for radiographic images, because psychophysical compression techniques assume prior knowledge of display characteristics and viewing conditions. The most common alternative is to use uniform quantization. The justification for this rests on the assumption that there is no a priori reason to believe that certain spatial frequencies are more important than others.

In our interpretation, the JPEG standard implies that any compression process is compatible with the standard if the encoded images it produces can be decoded with a standard JPEG decoder. Specifically, this permits various kinds of preprocessing to be applied to the input image data before the actual compression. Such preprocessing can improve the overall results of the compression/decompression cycle. For example, we have shown⁷ that when root mean square error (RMSE) is used as the measure of image fidelity, at sufficiently large compression ratios, there are significant advantages to applying a noise-removal filter to the image data before compression.

Another aspect of this preprocessing, which is somewhat unique to mammography, involves the segmentation of the image. Much of the area in a typical digitized mammogram corresponds to background pixels rather than to tissue pixels. These background pixels contain noise that is typically difficult to compress. To optimize compression in this case, it is important to minimize the amount of data required to represent these background pixels in the encoded image. This can be done in a JPEG-compatible manner by first cropping the image to the smallest rectangular area that contains all of the tissue, and then identifying the remaining background pixels and replacing them with a constant value.

With these considerations in mind, in our laboratory we have developed and begun testing software for JPEG-compatible compression of digitized mammograms.

MATERIALS AND METHODS

As described in more detail below, our compression software is consistent with the extended 12-bit version of the JPEG standard and uses a set of preprocessing routines designed specifically for mammograms. This software was written in C to be transportable, but all of the processing reported in this paper was performed on a standard 33-MHz 486 personal computer. We have tested this software by using it to compress a set of digitized mammograms at various levels of quantization, and then evaluating the quality of these compressed images by performing a just-noticeable difference (JND) study.

Preprocessing. Before applying the JPEG compression algorithm, the image data is preprocessed to improve its compressibility. This preprocessing operation is divided into two phases; first the image is segmented and cropped and the background pixel values are modified to minimize the storage requirements for the background, and then a noise-removal filter is applied to the tissue pixels.

We begin the segmentation process by automatically determining a threshold value from the histogram of the digitized source image that indicates the transition between background values and tissue values. This threshold value is used to classify pixels in the image as either tissue or background so as to produce a two-valued mask corresponding to the tissue-background separation. The thresholded image normally consists of a large contiguous region corresponding to tissue, possibly containing small holes, as well as smaller isolated clusters of points from the noisier background regions.

An initial “seed” point in the tissue area is automatically selected and grown to encompass the largest possible connected region. This produces a binary mask matching the tissue pixels in the source image. This mask is expanded by 15 pixels—ie, any pixel that is within 15 pixels of a tissue pixel is appended to the mask. This expansion is effected by convolving the binary mask with a 31- × 31-pixel uniformly weighted kernel and then assigning all nonzero pixels the value 1.

We then convolve this binary mask with a 17- × 17-pixel uniformly weighted kernel to smooth the edge between the mask (pixels = 1) and background (pixels = 0). This expanded and smoothed mask, whose pixel values represent an interpolation factor λ , has a value of 1 for every soft-tissue pixel and every background pixel within 7 pixels of a tissue pixel, and goes smoothly to zero over a distance of 16 pixels as the distance from tissue pixels increases. This mask and the source image are both cropped to a rectangular area that excludes as many zero pixels as possible while retaining all nonzero pixels.

A constant value, which is to be used in modifying background pixels, is determined by averaging the background pixels that are near the skin boundary. Finally, the output image is created pixel by pixel by interpolating between the source image and the constant value using the

DATA COMPRESSION OF MAMMOGRAMS

formula

$$\text{output} = \lambda \cdot \text{source} + (1 - \lambda) \cdot \text{constant} \quad (1)$$

The resulting image has the following characteristics: (1) any 8- × 8-pixel block that contains a tissue pixel will remain unchanged from the source image, eliminating the possibility that the segmentation process will alter the effect of compression on any tissue pixel; and (2) background pixels will have been modified to change in a smooth and continuous manner from their original values to the prescribed constant value as a function of distance from the nearest tissue pixel, thus reducing the possibility that the segmentation process will introduce an edge artifact at the tissue/background boundary.

The second preprocessing phase involves the application of a filter to the tissue area of the image. The particular filter tested here is a nonlinear order filter^{7,8} that was designed to modify mainly pixels with large noise components while leaving the majority of pixels unchanged. This filter operates as follows. The source image is first decomposed into a high-frequency component and a low-frequency component by unsharp masking—a process whereby a low-frequency version of the source image, obtained by smoothing the source, is subtracted from the source image to produce an edge-enhanced (high-frequency) version of the source. Pixel values in each 3- × 3-pixel block of the high-frequency component are sorted. If the center pixel of the block is the highest value in the block, it is assigned the value of the next lower pixel. Similarly, if it is the lowest value, it is assigned the next higher value. Otherwise, the pixel is left unchanged. This results in a rather innocuous process of eliminating one pixel maxima or minima from the high-frequency component, while leaving most pixels unchanged. The small number of pixels changed are likely to represent noise, as their values are either greater or less than the values of all their immediate neighbors. Microcalcifications in the image are generally preserved because they rarely consist of a single pixel. Finally, the filtered high-frequency component is added back to the low-frequency component to produce the filtered source image.

These preprocessing operations require two convolutions with uniform kernels, two applications of a threshold, a region growing step, an interpolation step, and application of the nonlinear filter. In our implementation, which does not require manual intervention, all of these steps are performed in approximately one third of the time of the compression itself.

Image compression. The JPEG compression algorithm used in this study is a software package written and tested in our laboratory that implements the 12-bit version of the extended JPEG standard. For this study, Huffman encoding was used to encode the quantized coefficients and all compression ratios were based on this. The Huffman tables were derived from the statistics of each individual quantized image rather than on the ensemble statistics. Signaling information was not included in the code size when calculating compression ratios.

Results reported in this paper are based on uniform quantization of the frequency coefficients. As discussed below, any quantization scheme that preferentially degrades the high-frequency components (ie, most of the

psychophysical quantization schemes) may be contraindicated in the compression of mammographic images.

Evaluation of image-compression technique. In an effort to understand the viability of the methods described above, we carefully selected eight high-quality cases that spanned the range of image characteristics customarily encountered in mammography, with some preference being given to images containing subtle pathology. These cases were digitized and the digital data was compressed over a wide range of compression ratios by applying the above techniques.

The digitization process used a high-resolution, high-contrast sensitivity laser film digitizer (Lumisys, Sunnyvale, CA) that produces a scan matrix of 4,000 × 5,000 pixels for an 8- × 10-in film by digitizing at a 50-μm sampling interval. This pixel resolution results in a Nyquist spatial frequency of 10 cycles/mm, which preserves the signal resolution of the analog film. The modulation transfer function (MTF) at the Nyquist frequency is 30% in the fast-scan direction and 38% in the slow-scan direction. The 16-bit A/D converter of the digitizer permits a density measurement with an RMSE of less than 0.01. This represented less than one third of the noise present in the conventional film at densities exceeding 0.4.

Each digitized image was compressed at five different compression ratios. Because it is the degree of quantization rather than the compression ratio itself that determines the degradation of an image by compression, the quantization factor was used as an independent variable and not the actual compression ratio. The five quantization factors we applied were 40, 60, 80, 100, and 120, which produced average compression ratios between 15:1 and 60:1. The lowest quantization factor is at a level below which it is not expected that one could detect any effect. The highest quantization factor produced a mean compression ratio of 60:1, which is higher than what is required to permit the efficient handling of mammographic images with current digital technology, and it is in the range where studies of other algorithms applied to other image types have shown significant deterioration in image quality.^{9,10} Note that these particular quantization factors are only appropriate for images digitized at the resolution and with the noise characteristics under consideration in this study.

All images used in this study, both the compressed versions as well as the original digitized data, were printed on film with a laser film printer (Eastman-Kodak, Rochester, NY). These laser-printed films were used for all image comparisons. It was not possible for us to perform a meaningful comparison of the laser-printed images to the original (nondigitized) images because our laser printer was only capable of printing at a pitch of ~80 μm/pixel, and this resulted in substantial (1.6 ×) magnification of the laser-printed images. However, comparing two images that have both been enlarged to the same degree is possible, and if the enlargement had any effect, we believe it would have been to make it easier for readers to discriminate between noncompressed images and compressed images. The overall digitizer-processor response was calibrated to accurately duplicate the densities and contrast in the original film. Noise contributed by the laser printer is substantially less than image noise caused by quantum mottle and film granularity in the original film.

Table 1: The Effect of Image Segmentation on Tissue Block Representation (bits per block)

Image	% of Area Representing Tissue	Bits per Tissue Block (no preprocessing)	Bits per Tissue Block (after segmentation)	Improvement Factor
1	51.1	8.6	30.1	3.5
2	52.9	8.5	27.0	3.2
3	70.5	9.1	32.3	3.5
4	71.7	10.0	28.0	2.8
5	72.4	9.4	23.6	2.5
6	56.8	7.6	26.5	3.5
7	70.7	24.2	27.4	1.1
8	67.0	18.0	22.2	1.2

From the eight originals, which had each been compressed at five compression ratios, a set of 40 randomized pairs of images, each consisting of one laser-printed noncompressed image and one compressed version of the original, were assembled. Readers were asked to view the pairs side by side and were forced to choose the image they believed to have been compressed. Readers were allowed to spend as much time as desired on each pair. The reading environment was equivalent to that normally used for reading mammograms and readers were permitted to use magnifying lenses.

Altogether, 20 readers participated in these readings. They included radiologists experienced in mammography as well as physicists and engineers specializing in medical imaging.

RESULTS

The performance of our compression system is somewhat image dependent, but for the ensemble of images reported on here, we averaged about 20 s/Mbyte to preprocess and compress source data. Because decompression does not involve any steps similar to preprocessing, we were able to perform it at a rate of 15 s/Mbyte of output data. Although these speeds are not acceptable for a clinical picture archiving and communication system (PACS) environment, we believe they can be easily improved by adopting hardware optimized for the task.

A summary of the impact of image segmentation on the number of bits needed to represent tissue blocks is presented in Table 1. All images included in this table had previously been cropped to a rectangular area whose border was within 1 cm of tissue pixels in each dimension. Column 2 gives the fraction of the cropped image occupied by tissue pixels. Columns 3 and 4 give the average number of bits used to represent each 8- × 8-pixel block of tissue pixels before and after application of the segmen-

tation process, for an overall compression ratio in both cases of 40:1. It can be seen from this table that our segmentation process increased the number of bits used to represent each tissue pixel by a factor of 2.7 on the average despite the fact that the background represented only 35.9% of the image area.

From approximately 800 observations in the JND experiment, average observers correctly detected 42%, 55%, 47%, 61%, and 75% of the images for the 15:1, 23:1, 34:1, 45:1, and 60:1 compression ratios, respectively. However, when we looked at the performance of individual readers, we found that there were two readers who were particularly good at making the discriminations required in this study. These readers were a physicist and an electrical engineer who were both specialists in image processing and were familiar with the particular artifacts caused by this type of image compression. These image-processing specialists averaged discrimination rates of 50%, 67%, 75%, 87%, and 100% for the above compression ratios. Their surprising consistency with each other and the monotonic trend of their performance led us to believe that we were actually measuring a meaningful threshold. A plot of the results of this JND study is shown in Fig 1.

DISCUSSION

Performance of compression process. The relationship between the compressibility of tissue, the compressibility of the background, and the relative areas between tissue and background

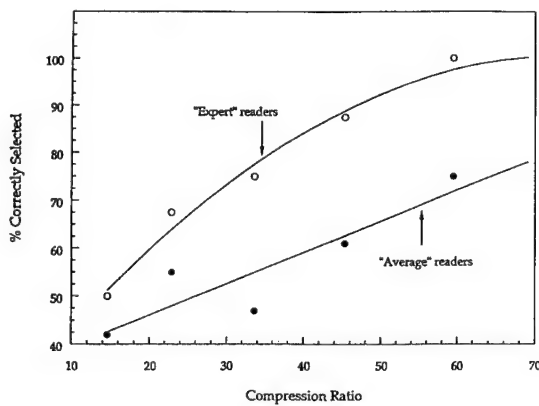


Fig 1. Performance of image-processing specialists and nonspecialists for the task of identifying compressed versus noncompressed images.

DATA COMPRESSION OF MAMMOGRAMS

can be expressed as

$$C_t = \frac{A_t}{\frac{A_t + A_b}{C} - \frac{A_b}{C_b}}, \quad (2)$$

in which C_t and C_b are, respectively, the compression ratios for A_t and A_b , the areas corresponding to tissue and background, and C is the overall compression ratio for the image. The potential improvement factor in the number of bits per tissue pixel that can be achieved through segmentation, assuming the background is compressed to a negligible size after segmentation, is

$$\frac{1}{1 - \frac{A_b}{A_t + A_b} \cdot \frac{C}{C_b}}, \quad (3)$$

where C_b is the compression ratio of the background without segmentation. In all cases, after segmentation we were able to compress the background at a ratio of 256:1, which corresponds to using 3 bits to represent each 8- \times 8-pixel block. Theoretically in some unusual cases, it would be possible to use only 2 bits per block, but this is an absolute limit for the JPEG algorithm (sequential discrete cosine transform [DCT] and Huffman encoding). The actual improvements in bits per tissue pixel are indicated in Table 1, column 5.

Note that images 7 and 8 behaved somewhat differently than the other six images. The backgrounds of these images were so dense that they were beyond the range of our digitizer. Consequently, many background pixels values were saturated at the maximum output of our digitizer, and hence, the apparent noise in the background was greatly reduced. Saturation of the background had much the same effect as our segmentation process, but has the potential to also alter tissue pixels in an undesirable way. We have included these particular images after verifying that the tissue pixels themselves were not saturated.

For images 1 through 6, our segmentation process increased the number of bits used to represent each tissue pixel by a factor of 3.2 on the average. If images 7 and 8 are also included, this effect is reduced to 2.7. The average area occupied by tissue pixels in cropped images 1

through 6 was 62.6%. It can be seen that for images in which the background is not saturated, the average improvement in bits per tissue pixel is much larger than what would be suggested simply by the relative areas occupied by the tissue pixels and background pixels.

We illustrate what happens during the segmentation process by using image number 6 from our study as a specific example. This image, which is partially shown in Fig 2, is typical of what we have observed in general. Initially, this mammogram was digitized to a 12.3-Mbyte file. Cropping reduced this by 5.7% to 11.6 Mbyte, and of this file, 56.8% of the pixels corresponded to tissue.

A plot of the compressibility of various regions of this image, which are identified in Fig 2, is presented in Fig 3. The independent variable on this graph, the quantization factor, is specified at the time of compression and directly controls the loss of information during the compression process. It can be seen that different regions of the image vary widely with respect to their compressibility and that the background is significantly less compressible than either of the tissue regions. In many cases such as this one, because the background is very noisy, it is the least compressible part of the image. When the nonsegmented version of this image was compressed at a ratio of 25:1 (0.48 bits per pixel), the compression ratio of the background was only 14.9:1 compared with 51.8:1 (0.23 bits per pixel) for the tissue pixel. The encoded file contained 0.464 Mbyte of data of which 0.337 Mbyte was needed to describe the background and the remaining 0.127 Mbyte represented tissue. In other words, despite the fact that the background was only 43% of the source image, more than 72% of the data in the encoded file was used to describe the background. After the image was preprocessed and compressed at the same 25:1 compression ratio, the constant background in the segmented image was now compressed at a ratio of 256:1 (.05 bits per pixel) and the tissue area was compressed at a ratio of 14.8:1 (0.81 bits per pixel). The background was reduced to only 0.02 Mbyte or about 4% of the encoded data. The net effect was that segmentation increased the amount of data used to represent tissue pixels by a factor of 3.5. Figure 4 compares the overall compress-

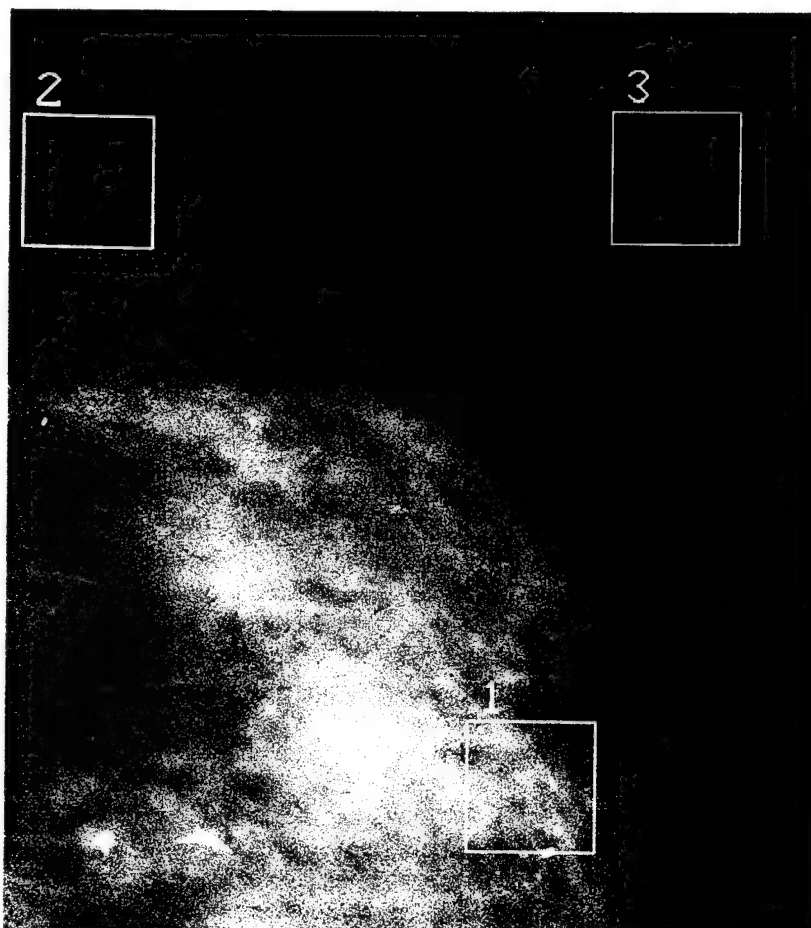


Fig. 2. Image showing the three typical regions of interest in different areas representing tissue and background.

ibility of the segmented image to that of the nonsegmented image. The compressibility of a chest image is also included for comparison.

Figure 5 shows in more detail the relative number of bits per tissue pixel between the

segmented and nonsegmented images. The actual pattern of the compressibility of various parts of the image is also of interest because it provides information that eventually will be needed for optimizing the relative compression

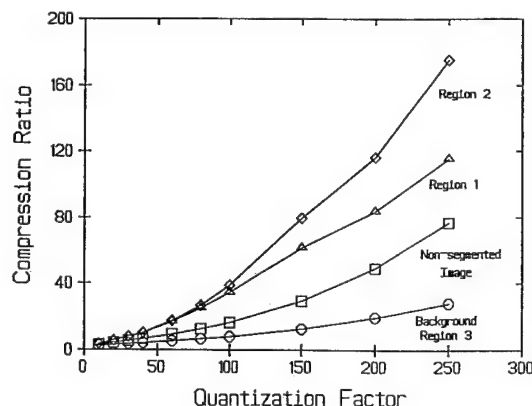


Fig. 3. Comparison of the compressibility of the three regions marked in Fig 2, with the compressibility of the image as a whole.

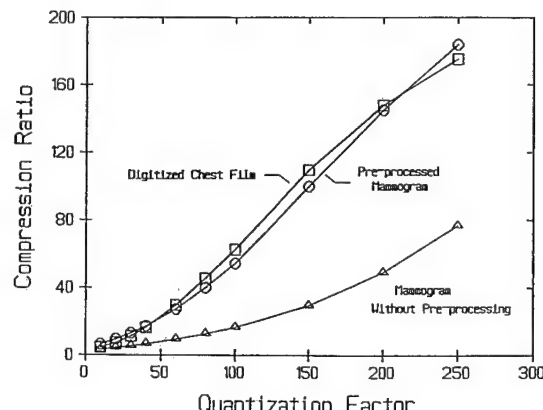


Fig. 4. Comparison of the compressibility of mammograms with and without preprocessing to the compressibility of digitized chest images.

DATA COMPRESSION OF MAMMOGRAMS

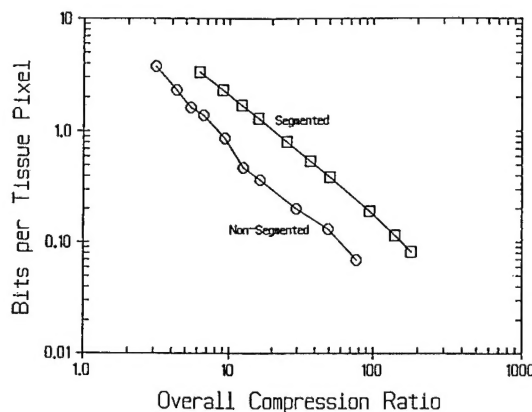


Fig 5. Comparison of the mean number of bits used to represent a tissue pixel for segmented versus nonsegmented images.

of different tissues. Figure 6, A and B show the pattern of bits per pixel with and without preprocessing. It is clear from a comparison of these images that preprocessing results in a dramatic shift, from bits being used to represent background to being used to represent tissue. One further observation from Fig 6B is that a large fraction of the bits used to represent tissue are in fact used to represent only the regions near skin. This observation is consistent throughout the ensemble of images we have studied to date. We believe it is mostly caused by the low compressibility of the high-frequency structures in the near-skin regions and to a lesser extent caused by the high density of the skin areas on the original films that produces increased digitizer noise. This can be seen in Fig 7, which

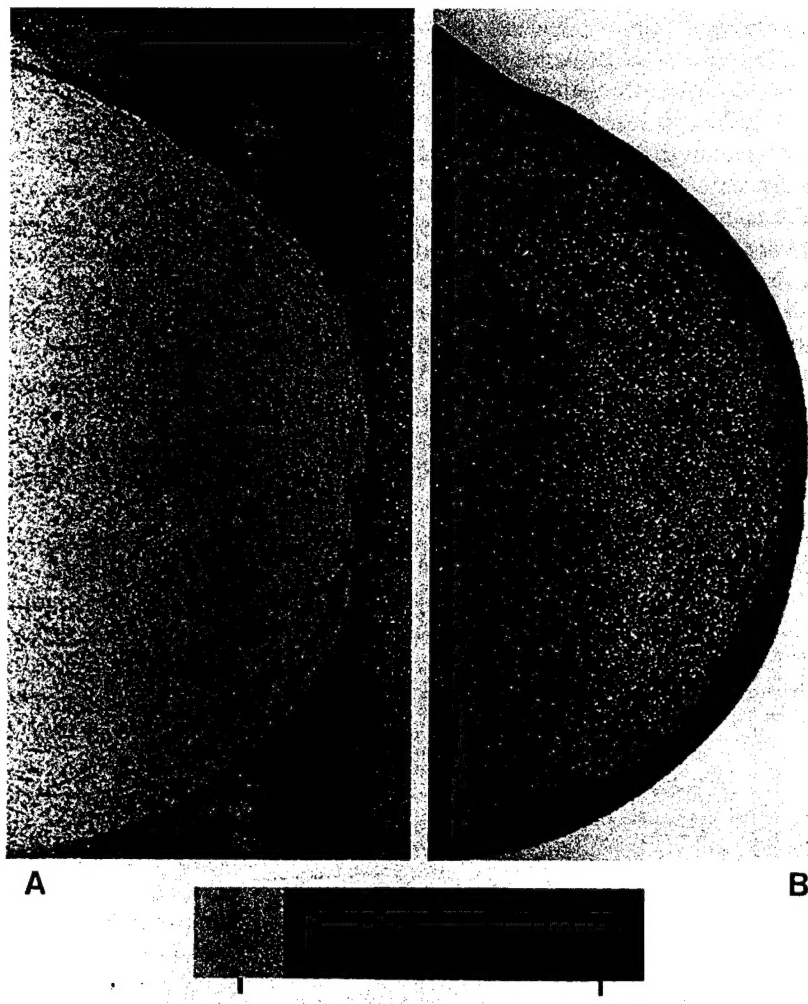


Fig 6. Images of bits per block before segmentation (A) and after segmentation (B) for an image compressed at 40:1.

relates the number of bits per pixel to film density for a fixed quantization level, for reasonably flat areas of an image. The increasing trend as a function of optical density is caused by the increasing noise of the digitizer as film density increases. Also shown in Fig 7 are measurements of the compressibility of skin areas as a function of density. These points are clearly above the line. We have observed that this low compressibility of the skin areas also holds for storage phosphor (computed radiography) images despite the very different noise characteristics of these images.

Future updates to the JPEG standard are likely to contain provisions for adaptive quantization. When this happens, it will be necessary to address the issue of the relative number of data bits that should be allocated to represent each particular type of tissue.

Effect of filtration. The effects of applying the nonlinear filter to mammogram number 6 is shown in Fig 8. Although the filter only changed 6.7% of the pixel values, it seemed to provide a net benefit at the higher compression ratios. Its behavior was comparable with what was achieved when a similar filter was applied to the compression of chest images.⁷ Figure 8 shows the RMSE for the compression of the filtered source along with the RMSE for the compression of the nonfiltered source as they depend on the compression ratio. It can be seen that at low compression ratios, the RMSE of the filtered image is higher because of changes in the image caused by the filter, but at higher compression

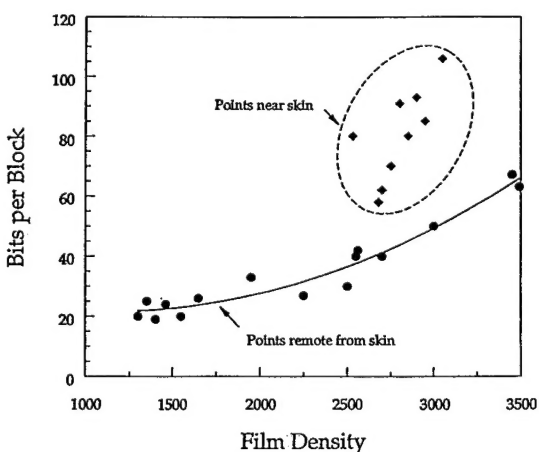


Fig 7. Plot of compressibility of different "nonskin" tissue regions as a function of film density (line). Also included are data from different points in the skin region.

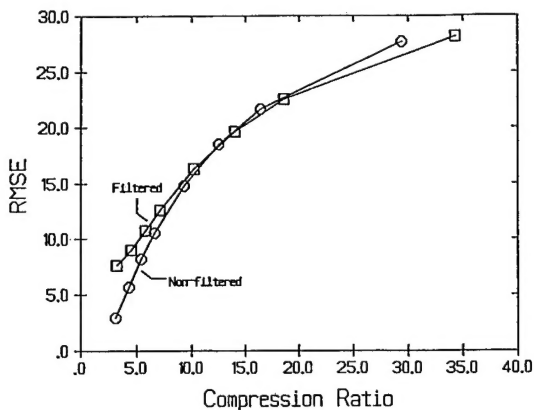


Fig 8. RMSE resulting from nonlinear filtration as a function of compression ratio. Results for both the filtered and nonfiltered image are shown.

ratios, the errors caused by compression overwhelm the error caused by filtration and become predominant. The compression-induced errors are consistently smaller for the filtered image than for the nonfiltered image, and at higher compression ratios, the filtered image actually deviates less from the source image. This behavior persisted across our image set, but was found to be image dependent. It is our view at this time that filtration of this sort is advantageous at compression ratios above 20:1, but it remains to be tested in diagnostic performance studies.

Effect of segmentation and cropping. In general, for all of our images, preprocessing the digitized data made a dramatic improvement in compressibility. This improvement can be attributed, for the most part, to the benefit of segmentation. It is actually the degree of compression of the image area corresponding to tissue pixels, or the number of bits per tissue pixel, rather than the compression ratio for the entire image array, that directly determines the impact of compression on the diagnostic quality of mammographic images. In mammography, there is wide variation from case to case in the proportion of the film occupied by tissue pixels. In all cases, after segmentation and cropping, the background will be compressed at a very high compression ratio, whereas the tissue pixels are compressed at a more modest ratio.

If images are not segmented, then cropping is particularly beneficial. However, if the images are segmented by the above procedure, the benefit of cropping is largely neutralized by the

DATA COMPRESSION OF MAMMOGRAMS

efficiency of the segmentation process in increasing the compressibility of the background. Nevertheless, cropping can be useful, because when the image is reconstructed, it will retain its size before encoding. Maintaining excessive background pixels could have adverse effects on the time required to encode and decode the image as well as on other system components such as image displays.

Preservation of image quality. Much of a mammographic image does not contain appreciable high-frequency information, but the need to preserve microcalcifications with dimensions of less than 100 μm , which sometimes appear in mammographic films, may require that we digitize mammograms at 50 μm . This has the effect of oversampling most of the image—ie, the actual information content of the digitized mammogram is much less than the size of the image matrix would suggest.

It does not require severe quantization to achieve a high compression ratio on areas that do not contain high-frequency information. The remainder of the image, such as areas containing microcalcifications or the skin, is not as compressible, but these areas generally comprise such a small fraction of the total area that they have minimal impact on the compression ratio. Together, these factors imply that it may not be necessary or desirable to preferentially degrade the higher-frequency components in the quantization process to achieve high compression ratios, and consequently, it is possible to preserve features such as microcalcifications during the compression process.

In comparing the compressibility of mammograms to that of chest images, we found that preprocessed mammograms are very similar to chest images in compressibility; however, unprocessed mammograms are much more difficult to compress than chest images. We have included a plot in Fig 4 that was derived from a

previous study⁷ of the compression ratio of chest images versus the quantization factor. The chest image had been digitized at 100- μm resolution with 12 bits of dynamic range. At each level of quantization, the RMSE for the chest image was similar to the RMSE for mammograms compressed with the same quantization factor.

Observer performance. When the differences between images are small, it is possible that readers can detect the difference, but still not be able to tell which image is compressed. The key to differentiating between images at the lower compression ratios seemed to be the presence or absence of blocking artifact. For the compression techniques we applied in this study, blocking artifact becomes noticeable before any degradation of image resolution is obvious. Blocking artifact could be detected by image-processing specialists and nonspecialists alike, but the nonspecialist readers were more likely to misinterpret it. It is clear from discussions with some readers upon completion of their readings, that when the blocking artifact was barely visible they sometimes mistook it for actual image information and assumed the image with the artifact was the noncompressed image. The two best readers seemed to be able to avoid this mistake.

The JND study presented here is not intended to address the question of the impact of compression on diagnostic performance. Its purpose was merely to give us an opportunity to test the feasibility of the techniques we believe are appropriate for the compression of mammographic data, and to identify the range of compression ratios that merit further study. There are many possibilities for further refinements, particularly in the area of preprocessing the data, that are within the constraints of the standard, and these will likely extend the useful range of compression ratios.

REFERENCES

1. Joint Photographic Experts Group (JPEG): JPEG Technical Specification, Revision 5 (Document No. JPEG-8-R5 or JTC1/SC2/WG8 N933). ISO Central Secretariat, 1990
2. Hudson GP, Yasuda H, Sebestyen I: The international standardization of a still picture compression technique. Proc IEEE Global Telecommunications Conference & Exhibition, vol 2, November 28-December 1, 1988, pp 1016-1021
3. Wallace G, Vivian R, Poulsen H: Subjective testing results for still picture compression algorithms for international standardization. Proc IEEE Global Telecommunications Conference & Exhibition, vol 2, November 28-December 1, 1988, pp 1022-1027
4. Daly S: Application of a noise adaptive contrast sensitivity function to image data compression. Proc SPIE 1077:217-227, 1989
5. Rabbani M, Daly S: An optimized image data compression technique utilized in the Kodak SV9600 still video transceiver. Proc. SPIE 1071:246-256, 1989

GOOD, MAITZ, AND GUR

6. Ngan KN, Leong KS, Harcharan S: Cosine transform coding incorporating human visual system model. Proc SPIE 707:165-171, 1986
7. Good WF, Gur D: Quantization techniques for the compression of chest images by JPEG type algorithms. Proc SPIE 1652:114-121, 1992
8. Boncelet CG: Some uses for order statistic filtering in image compression. Proc SPIE 1247:51-57, 1990
9. Ishigaki T, Sakuma S, Ikeda M, Itoh Y, Suzuki M, Iwai S: Clinical evaluation of irreversible image compression: Analysis of chest imaging with computed radiography. Radiology 175:739-743, 1990
10. MacMahon H, Doi K, Sanada S, Montner SM, Giger ML, Metz CE, Nakamori N, Yin F-F, Xu X-W, Yonekawa H, Takeuchi H: Data compression: Effect on diagnostic accuracy in digital chest radiography. Radiology 178:175-179, 1991